2017

Magnetic Petrophysics of the Vulcan Iron Formation (Michigan, USA)

Matthew Laird
Michigan Technological University, mslaird@mtu.edu

MAGNETIC PETROPHYSICS OF THE VULCAN IRON FORMATION (MICHIGAN, USA)

By

Matthew Laird

A THESIS

Submitted in partial fulfillment of the requirements for the degree of

MASTER OF SCIENCE

In Geophysics

MICHIGAN TECHNOLOGICAL UNIVERSITY

2017

This thesis has been approved in partial fulfillment of the requirements for the Degree of MASTER OF SCIENCE in Geophysics.

Department of Geological and Mining Engineering and Sciences

Thesis Advisor:	*Aleksey Smirnov*
Committee Member:	*Will Cantrell*
Committee Member:	*Jeremy Shannon*
Department Chair:	*John Gierke*

Table of Contents

List of Figures

List of Tables

Acknowledgements

There are many people that need to be thanked for their contributions to this project.

First, I would like to thank my advisor Aleksey Smirnov for his immense contribution to this project. Our discussions over the course of the project, sampling assistance, writing advice, and overall drive were crucial to this projects success.

My committee, for their observations and recommendations on this project

My girlfriend Jenna Dahlstrom needs to be thanked for her continued support when things were going well and when things were going poorly.

Marine Foucher, Leo Surovitsky, Jacob Tresnak, and Katie Bristol for their continued advice and expertise in all aspects of the project.

My Parents (all six of them) and Brothers and Sisters (all nine of them) for their support and belief in me that I could finish this project and my Masters Degree.

The Geology Department of Michigan Technological University for all the help provided during my time with them.

My friends, for being there for me.

Lastly my Pets; Whisper, Jules, Vincent, Butters, Tom, Chant, Momo, Mandy, Ruby, Amos, Kenny, Tracker-Boon, and Harley. They know what they did…

Abstract

A detailed investigation of magnetic properties of the iron-bearing Traders and Curry members of the ~1.88 Ga Vulcan Iron Formation (Michigan's eastern Upper Peninsula) was conducted using natural remanent magnetization, low-field magnetic susceptibility, anisotropy of magnetic susceptibility, thermomagnetic and magnetic hysteresis, and first-order reversal curve analyses. A set of samples were also investigated using electron scanning microscopy and energy dispersive spectrometry. Contrary to previously accepted views, our results indicate that the Traders and Curry members have substantially different properties. The older Traders member is a typical banded iron formation characterized by a higher relative amount of magnetite and stronger magnetic susceptibility. The younger Curry member lacks consistent banding and is characterized by a lower magnetite-to-hematite ratio and weaker magnetic susceptibility. These observations are important for interpretation of future aeromagnetic surveys over the Vulcan Formation and may be useful for understanding the depositional regimes and environmental conditions during the late Paleoproterozoic.

1. Introduction

Iron formations represent a subclass of iron-rich (containing >15% of iron) sedimentary rocks composed of layered, bedded, or laminated rocks, in which iron oxide or sulfide minerals are commonly interlayered with quartz, chert, or sometimes carbonate (e.g., Gross, 1980). Practically all known iron formations were deposited in the late Archean and Proterozoic with two peaks of deposition activity at ~2.7-2.4 Ga and ~1.9-1.8 Ga (e.g., Klein, 2005). Although the formation processes of iron formations are diverse and many of their aspects remain unresolved, it is generally accepted that the low oxygen content in the Earth's atmosphere during those periods allowed great quantities of iron to be transported in its soluble, reduced (ferrous) form into broad, shallow marine environments where it was oxidized to its insoluble (ferric) form and precipitated (e.g., Bekker et al., 2010).

Precambrian iron formations are divided in two types depending on their depositional environment (e.g., Gross, 1980). The first, Algoma-type, is represented by relatively small (in both volume and spatial extent) iron formations interlayered with or stratigraphically linked to submarine-emplaced volcanic rocks in greenstone belts and, in some cases, with volcanogenic massive sulfide deposits (Bekker et al., 2010). The second, much larger Superior-type iron formations are formed in passive-margin sedimentary rock successions and generally lack direct relationships with volcanic rocks.

The iron formations are also divided into two classes based on their texture – banded iron formation (BIF) and granular iron formation (GIF). BIFs usually consist of alternating layers of silver to black iron oxides such as magnetite or hematite with layers of reddish iron-poor shale (a fine-grained, clastic sedimentary rock composed of a mix of flakes of clay minerals and tiny fragments (silt-sized particles) of other minerals, especially quartz and calcite) or chert (a fine-grained sedimentary rock composed of microcrystalline or cryptocrystalline silica). Layers can vary in thickness from a few millimeters to a few centimeters. Some BIFs, however, may locally lack visible laminations (banding) and exhibit granular textures. On the other hand, GIFs lack even, continuous bedding but may contain discontinuous layers of iron-rich and silica-rich material (Gross, 1980). GIFs contain granules composed of chert and iron oxide, iron carbonate, or iron silicate. The

granules are considered detrital, with some (both well-rounded and angular) being derived by sedimentary reworking of iron-rich mudstone and arenite (Simonson and Goode, 1989). It is generally accepted that BIF deposition occurred in deep water while GIF deposition occurred above storm- and fair-weather base. Both varieties, especially for large formations, are thought to be formed in open-marine environments during high sea level (e.g., Simonson and Hassler, 1996).

Age-wise, BIFs are dominant in Archean to earliest Paleoproterozoic successions (~2.7-2.4 Ga), whereas GIFs are much more common in Paleoproterozoic successions (~1.9-1.5 Ga) which probably reflects environmental changes affecting the depositional regimes (e.g., Bekker et al., 2010). The deposition of giant iron formations has been found to be coeval and genetically linked to, time periods when large igneous provinces (LIPs) were emplaced (Abbott and Isley, 2002). For example, the deposition of giant Superior-type BIF in South Africa, Australia, Brazil, Russia, and Ukraine between ~2.6 and ~2.4 Ga have been related to global mafic magmatism when construction of the first large continents changed the heat flux at the core-mantle boundary (e.g., Hoffman, 1987). The younger BIFs in this age range were deposited during the early stage of a shift from reducing to oxidizing conditions in the ocean-atmosphere system.

After the rise of atmospheric oxygen during the Great Oxidation Event (GOE) at ~2.4 Ga (e.g., Holland, 2002), GIFs became abundant in the rock record, compared to the predominance of BIF prior to the GOE (e.g., Bekker et al., 2010). However, the second peak in the iron formation deposition between ~1.9 and 1.8 Ga, well after the GOE, represents one of the unresolved questions because the free atmospheric oxygen should have promoted early oxidation of ferrous iron. Interestingly, this peak approximately corresponds to a mantle plume breakout event, suggesting a genetic link between the LIPs and iron formations. The relatively short duration of this period of intensive iron formation deposition is also enigmatic. The current models (e.g., Bekker et al. 2010) do not explain the mechanism that caused the ocean redox state prior to ~1.9 Ga to change back to anoxic ferruginous conditions and, subsequently at ~1.8 Ga, to either fully oxic or sulfidic conditions (Poulton et al., 2004). Iron formations generally disappeared at ca. 1.85 Ga, briefly reappearing at the end of the Neoproterozoic, again tied to periods of intense

magmatic activity and also, in this case, to global glaciations, the so-called Snowball Earth events (Hoffman et al., 1998).

Investigations of iron formations may provide important insights into the environmental conditions and depositional regimes that existed in the Neoarchean and Paleoproterozoic. A first-order observation that BIFs and GIFs have not formed during the Phanerozoic suggests that their formation conditions were substantially different and could have involved processes that have not been operating since the end of Precambrian. For example, the coincidence of cessation of the BIF/GIF formation with the appearance of multicellular life may suggest that biogenic processes could play an important role in the iron formation development. The former hypothesis is consistent with microfossils that have been found in the Paleoproterozoic BIF located in the Gunflint District of Ontario (Meurant, 2012). Therefore understanding iron formations may help understanding the Earth system during the Precambrian, including magmatism, evolution of the biosphere, and ocean composition (e.g., Huston and Logan, 2004; Holland, 2005).

In addition to their importance for understanding the early Earth evolution, iron formations are economically important being the source for giant hematite and martite-goethite iron ores (50-70 % Fe) that are the principal source of iron for the global steel industry (e.g., Bekker et al., 2010). Iron formations can blanket large lateral areas of several hundreds to more than a thousand kilometers and can be hundreds of meters thick. BIFs all around the world average around 38% iron content. These formations can contain mass quantities of iron ore, on a scale of 10^{14} to 10^{15} tons. Exploration and economical assessment of the mineral resources using geophysical methods requires knowledge of the physical properties of iron formations. In particular, an aeromagnetic survey represents the most efficient geophysical method for mapping iron formations to estimate their extent, structure and economic potential (e.g., Clark et al., 2014). Proper geologic interpretation of the aeromagnetic data however requires detailed and independent information on the magnetic properties of rocks (magnetic petrophysics).

This project has focused on the Paleoproterozoic Vulcan Iron Formation of the Menominee iron district that is located in the Dickinson County (the Upper Peninsula of Michigan) (Bayley et al., 1966) (Figure 1). The Vulcan Iron Formation represents the

second peak of iron formation development in the late Paleoproterozoic and hence is of a great interest in terms of understanding the Earth system conditions at that time including the mechanism of iron formation deposition. The last field-based geologic investigation of the Vulcan Iron Formation was reported in 1966 (Bayley et al., 1966), which included a limited amount of ground magnetic survey data. However, no rock magnetic data from the Vulcan Formation have ever been reported.

The overall goal of this project is to obtain a detailed rock magnetic characterization of the iron-bearing members of the Vulcan Iron formation (Michigan) suitable for petrophysical interpretation of high-resolution aeromagnetic data. This project is synergetic with the planned efforts of the United States Geological Survey to obtain a detailed aeromagnetic survey of the eastern Upper Peninsula of Michigan that includes the Vulcan Formation. The experiments included measurement of the low-field bulk magnetic susceptibility and anisotropy of magnetic susceptibility, magnetic hysteresis, natural remanent magnetization, and thermomagnetic analyses, as well as scanning electron microscopy and electron dispersive spectra analyses. Additionally, the new rock magnetic data contribute to an observational database that can be used for better understanding Precambrian Earth processes.

2. Geological Settings

2.1 Geologic Location

The Paleoproterozoic Vulcan Iron Formation of the Menominee iron district is located in Dickinson County (Eastern Upper Peninsula of Michigan) (Figures 1 and 2). The Vulcan Iron Formation comprises an upper iron-formation member (Curry Member), a middle siliceous, ferruginous slate member (Brier Slate Member; thickness 30-100 m), and a lower iron-formation member (Traders Member; thickness 20-60 m). At places, a local Loretto Slate Member overlies the Curry Member. The Vulcan Iron Formation conformably overlies the Felch Quartzite Formation which is mainly quartzose sericitic slate, quartzite, and conglomerate, some of which is ferruginous (Bayley et al., 1966). Together, the Vulcan Iron and Felch Formations form the Menominee Group which, in the studied area, is conformably overlain by the Michigamme Shale Formation of the Baraga

Group. Both the Menominee and Baraga Groups are members of the extensive Marquette Range Supergroup which covers much of the Western Upper Peninsula of Michigan as well as Northern Wisconsin (Cannon and Gair, 1970). The Vulcan Iron Formation has been correlated with the Negaunee Iron Formation of the Marquette district, the Ironwood Iron Formation of the Penokee-Gogebic district, and the Biwabic Iron Formation of the Mesabi district (Leith et al., 1935).

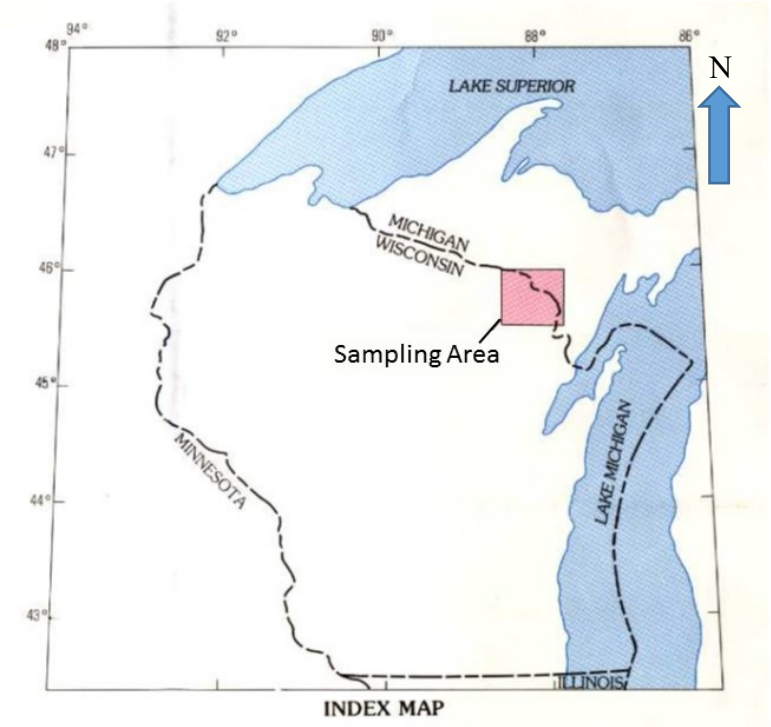

Figure 1: Geographic location of the sampling area (red box) in the Upper Peninsula of Michigan.

The studied area contains two major faults, the North Range Fault and South Range Fault, which were mapped as southside-up, high-angle reverse faults (Bayley et al., 1966) (Figure 3). The faults repeat an essentially south dipping homoclinal succession that internally is folded (Figure 2). The iron-bearing strata of the North Range of the

Menominee district is elevated along the north-verging South Range fault to form the south iron range (Figure 2).

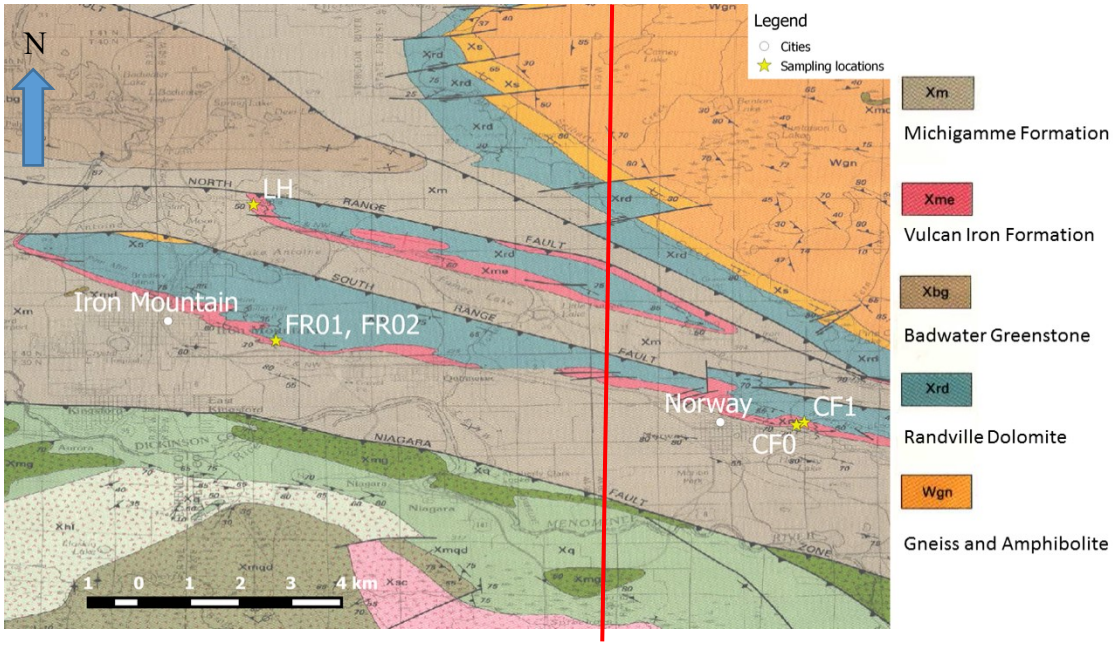

Figure 2: Sampling site locations for the Vulcan Iron Formation (Sims and Schulz, 1993). Red line showing cross-section.

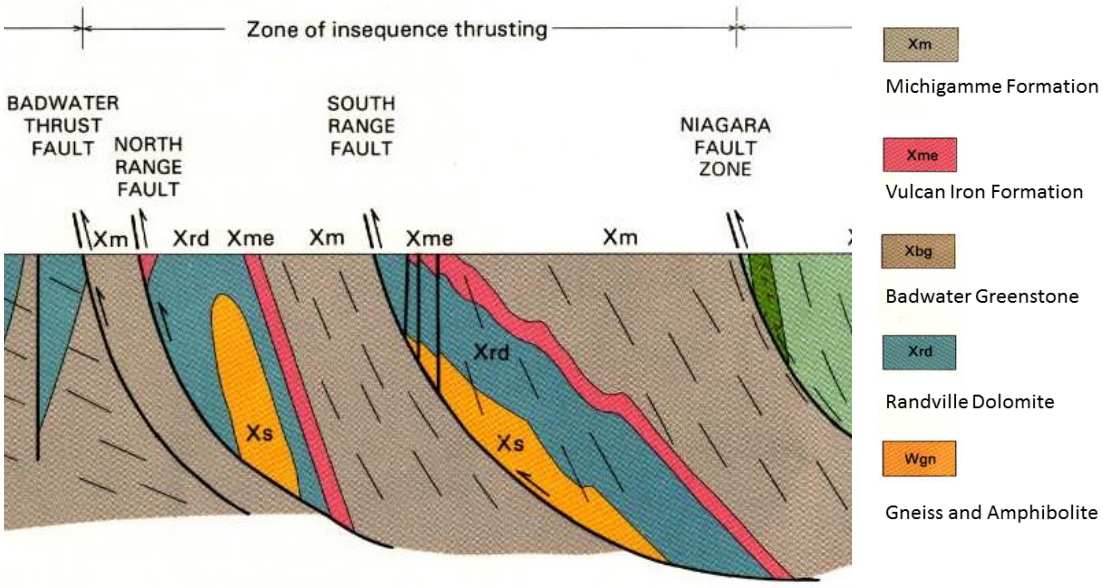

Figure 3:.N-S cross-section (Red line in Figure 2) of sampling area showing faults (Sims and Schulz, 1993).

The Vulcan Iron Formation is classified as a Superior-type Iron Formation due to its age, thickness, extent, and lack of associated volcanics (Gross, 1980). The iron-bearing members of the Vulcan Formation are chemical sedimentary rocks whose present characteristics reflect the chemical and physical conditions in the basin in which they were deposited and later diagenetic and metamorphic changes. The predominance of the magnetite and hematite indicates that the iron formations are of the oxide type indicating strong oxidation conditions prevailing at the ocean bottom during the deposition.

The iron-formations of the Vulcan formation are described as thin bedded and commonly laminated, but the thickness of the beds is not uniform with individual beds ranging from 1 mm to 30 cm. Typically, beds of granular jasper alternate with beds composed mainly of oxides of iron (hematite and magnetite) and minor amounts of crystalline quartz (and, rarely, dolomite and chlorite). The jasper beds are composed mostly of red jasper granules, specular hematite, magnetite and metachert (fine-grained crystalline quartz). In their primary state, the jasper granules are a mixture of amorphous silica and red iron oxide, and in their more characteristic crystallized state, the iron oxide is specular hematite and/or magnetite, and the silica is crystalline quartz (Bayley et al., 1966).

Iron formations composed dominantly of unaltered and altered jasper granules are both present in the Menominee district. The metamorphic grade in the area underlain by the iron formation, as determined from the mineralogy of slate and greenstone, ranges from low chlorite to low biotite grade (James, 1955). Although all degrees of crystallization of granules can be found throughout the iron formations in the studied area, crystallization has been most active in the areas of higher grade metamorphism (Bayley et al., 1966).

Deposition of the Vulcan Iron Formation is thought to have started around 1880 Ma, during the Penokean orogeny wherein the Pembine-Wausau terrane collided with the southern margin of the Archean Superior craton due to south direction subduction (Schultz and Cannon, 2007). This collision resulted in the formation of a shallow sea, where the Vulcan Iron Formation was deposited. The deposition likely occurred in a quiet-water condition as indicated by the presence of iron-silicate granules that grade laterally to oolites. However, there is debate as to the exact scenario surrounding the BIFs deposition - whether it was due to graben formation from an oblique collision with Wisconsin

magmatic terranes or back-arc spreading (Schulz and Cannon, 2007, Morey and Southwick, 1995).

2.2. Sampling Locations

Samples of both the Curry and Traders Members of the Vulcan Iron Formation were taken from four locations around the towns of Iron Mountain and Norway (Michigan) (Figures 1,2,4 and 6).

The Traders Member was sampled at one location (Sites FR01, FR02; 45.81161N 88.03291W) in a large excavation pit located on the north side of US-2 at the eastern part of Iron Mountain (Figure 5). Both core and block samples (see Methods) were taken from the eastern and western sides of the outcrop divided by a thin layer of slate in the center (Figure 5). The exposed BIF is vibrant with bands of red and grey and is easily distinguishable from a non-BIF slate layer that bisects the BIF at this location. The exposed rocks strike northwest and all have steep to subvertical dip to the south (the younging direction is to the south).

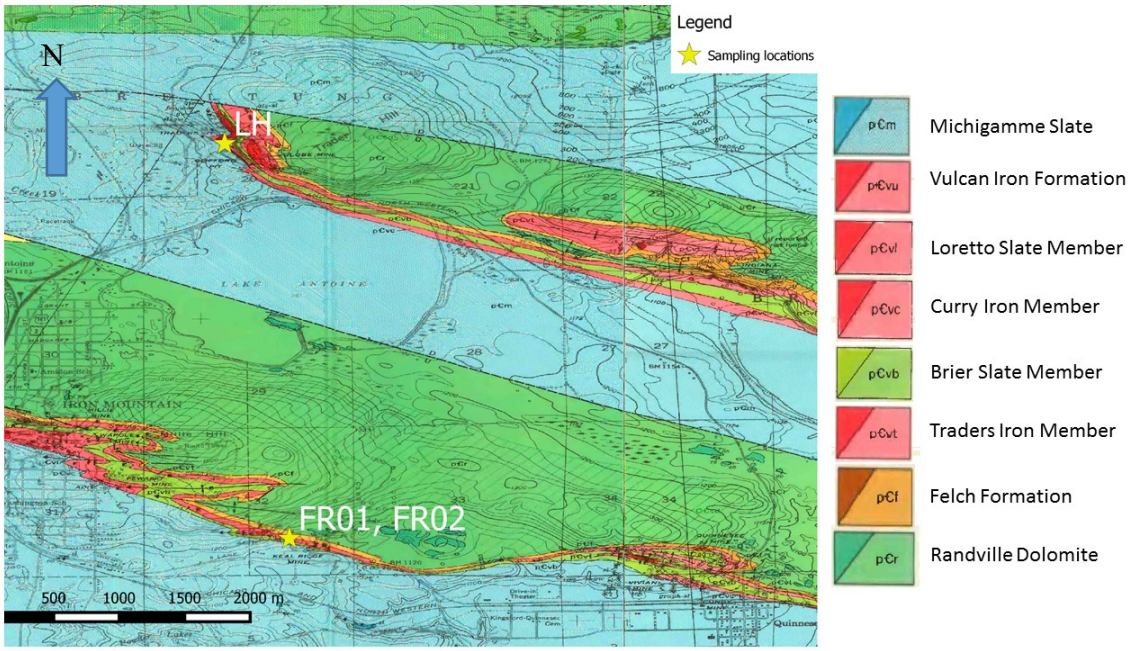

Figure 4: Sampling site locations near Iron Mountain, Michigan. Sites FR01 and FR02 are Traders Member outcrops. Site LH is a Curry Member outcrop.

Figure 5: The Traders Member sampling location (Sites FR01 and FR02). Exposed BIF is bright red and easily distinguishable from surrounding rocks (shown by the dashed line). Wall faces south and is around 4.5m tall.

The Curry member was sampled at three different locations. The first location (Sites LH01, LH02; 45.85063N 88.03935W), within the North iron range, was in the abandoned iron mine pit of the Globe Iron Co., in the northern part of Iron Mountain (Figure 4). The pit is now filled in with water and the Curry member is exposed along the ~100 m high northern and eastern walls of the pit (Figure 6). In order to sample the exposures, we had to use a canoe to cross the pit from its western accessible side. The BIF exposed at the Globe pit lacked pronounced banding but had a noticeable metallic shimmer which allowed for precise sampling. The exposed rock strikes northwest with an average dip of 70° to the south.

Figure 6: West-facing exposure of the Curry Member (Site LH) in an abandoned iron mine pit. The boat plus workers is about 1 m in height.

The Curry member was also sampled in two other locations within the South iron range, just east of Norway: a natural outcrop (sites LL01, CF01; 45.78960N 87.88751W) and what appears to be a small artificial (excavation) outcrop (site CF02; 45.78812N 87.88568W) (Figure 7). The natural outcrop is just off a highway 2 and around 10 m tall (Figure 8). The BIF located here does not appear to be banded but does distinguish itself from the surrounding rock with its characteristic metallic grey. The excavation outcrop is north of the natural highway outcrop. Visually, the rocks are not different from the previous outcrop. At both locations, exposed rocks strike due east and dip 55-60° to the south. Only block samples (no cores) were taken from both locations. Only one pilot sample was taken from Site LL01 which is not discussed in this thesis.

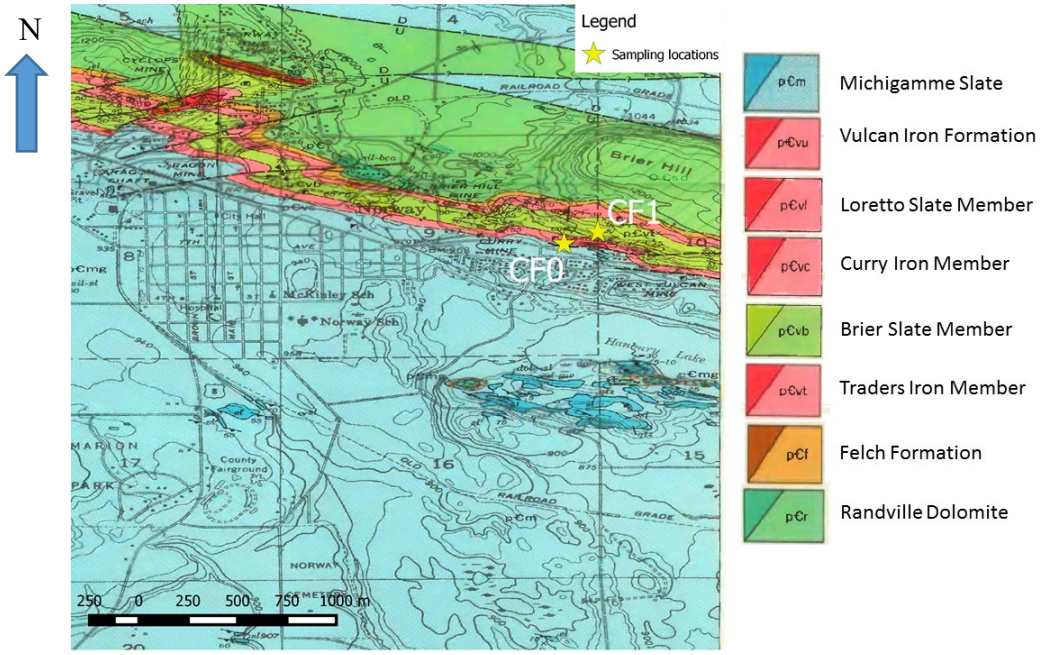

Figure 7: Western sampling site locations for the Curry Member (CF0 and CF1) near the town of Norway.

Figure 8: A south facing Curry Member outcrop (Site CF0) featuring difficult to distinguish iron-bearing formation.

3. Methods

3.1 Sampling and Sample Preparation

The sites were chosen with help from USGS scientist, Benjamine Drenth, and a local geologist, Tom Mroz. Seven core samples and four block samples were taken from the Traders Member rocks (FR01A, FR01B, FR01C, FR01D, FR01E, FR01F, FR01G, FR02A, FR02B, FR02C, FR02D). Nine block samples were taken from the Curry Member rocks (CF01, CF03, CF04, CF05, CF11, CF12, LH01, LH02, LL01). The core samples were taken with a portable Pomeroy Model D261-C gasoline powered drill with a diamond tipped Pomeroy BSS-1E drill bit (Figure 9a). The core samples were oriented with a Brunton compass, Pomeroy Orienting Fixture clinometer, and sundial in accordance with standard paleomagnetic procedures (Figure 9b). This method, however, proved difficult as the iron/silica-rich rocks are very hard and many drill bits were broken. It was therefore decided that taking block samples would be a simpler and more time-efficient method. Block samples were collected with care to make sure that the samples represented the rock

banding (when present). The block samples ranged in size from the size of a fist to the size of a football. These block samples were also oriented with the Brunton compass and sundial in accordance with standard paleomagnetic procedures similar to the core samples (Figure 9b).

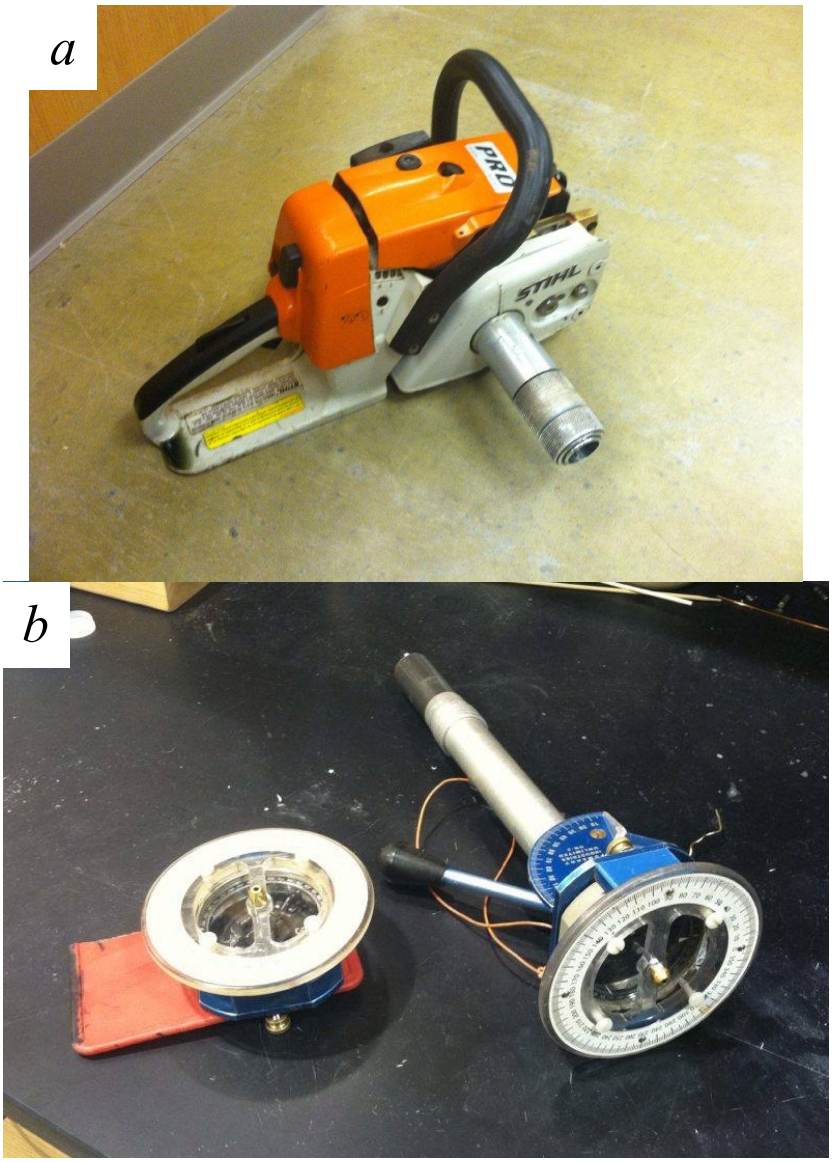

Figure 9: a) The portable gas powered drill used for sampling. b) Pomeroy Orienting Fixture clinometer and sundial (right) and a custom-made orienting fixture (left) used for orienting the core and block samples, respectively.

Specimens were prepared from the samples at the Rock Preparation Lab at Michigan Technological University. Standard cylindrical core specimens averaging 5 cm^3 or cubic bulk rock specimens averaging 4.5 cm^3 (from the core or block samples, respectively) were prepared for the natural remanent magnetization (NRM) and anisotropy of magnetic susceptibility (AMS) measurements (Figure 10a). To avoid the effects of weathering, the cylindrical specimens were cut from the bottom of the core, and the cubic specimens were cut from the block surface representing the deepest depth. For thermomagnetic analyses, a small amount (300–500 mg) of a sample was grinded into a fine powder using a sapphire mortar and pestle (Figure 10b). For magnetic hysteresis and first-order reversal curve (FORC) measurements, specimens (flat rock chips) averaging 1 mm^3 were produced from both the iron rich dark grey bands and iron poor red matrix bands (Figure 10b).

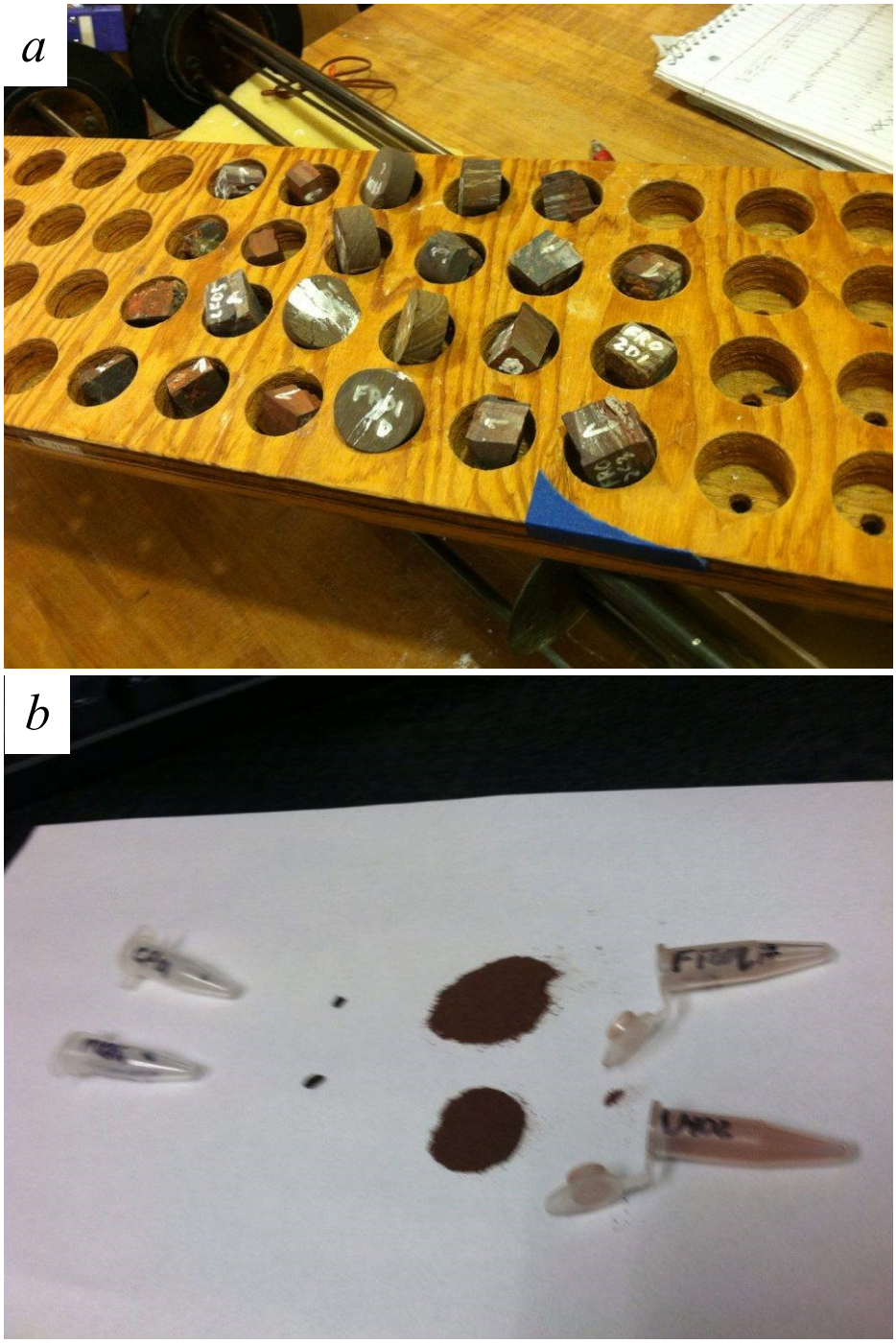

Figure 10: Examples of specimen used for experimentation. a) Cylinder and cubic specimens used in NRM and AMS measurements. b) From left to right, chips used in AGM and FORC measurements and powders used in thermomagnetic measurements.

3.2 Natural Remanent Magnetization (NRM)

The natural remanent magnetization (NRM) is defined as a magnetization that remains in a rock sample if it is placed in a magnetic field-free environment (e.g., Butler, 1998). The direction of NRM vector (J_{NRM}) is generally defined by the direction of Earth's magnetic field that existed at the time of rock formation (e.g., lava cooling or sediment deposition) but can deviate from the field direction if secondary components are present. In addition, the NRM vector directions can be modified by the sample's magnetic anisotropy. Knowing the strength and direction of NRM is important for correct interpretation of aeromagnetic anomalies.

The measurement of the natural remanent magnetization (NRM) of the specimens was done using a 2G Enterprises 760-R superconducting rock magnetometer (SRM) housed in the Michigan Technological University's Earth Magnetism Laboratory (Figure 11a). Before measurements, the blank SRM data files were created for data recording that included the information on the specimen's volume and the bedding elements for the Curry and Traders Member samples so that both the magnetization (the measured magnetic moment normalized by volume) and paleomagnetic directions in the geographical coordinates could be automatically calculated by the SRM software.

After measurement of the natural remanent magnetization, the component structure of NRM was investigated for selected specimens. First, the specimens were cycled through the Verwey transition at ~120 K (Verwey, 1939) by immersing them into liquid nitrogen for about two hours in order to reduce a viscous component carried by larger magnetite grains (Schmidt, 1993). After, the specimens were thermally demagnetized in a sequence of increasing temperature steps (starting with 20°C steps and ending with 5°C steps) using an ASC TD-48SC thermal specimen demagnetizer (Figure 11b) in an argon atmosphere. Progressive demagnetization was carried out until the magnetic intensity of the samples fell below noise level (usually 5% of initial magnetization) or until the measured directions became erratic and unstable (typically at 690 °C).

Figure 11: a) The 2G Enterprises 760-R Superconducting Rock Magnetometer at the Earth Magnetism Laboratory. b) The ASC TD-48SC Thermal Specimen Demagnetizer.

3.3 Thermomagnetic Analyses

In order to characterize the magnetic mineralogical composition of the samples, temperature dependences of low-field (200 A/m) magnetic susceptibility, κ(T), were measured using an AGICO (Advanced Geosciences Instruments Company) MFK-1FA magnetic susceptibility meter (Kappabridge) equipped with a CS-3 Furnace Apparatus (40-700 °C) and a cryostat (-192-0 °C) housed in Michigan Technological University's Earth Magnetism Laboratory (Figure 12). These measurements were conducted in three runs. The high-temperature run includes cycling the specimens between 40°C and 700°C. In addition, before and after the high-temperature thermomagnetic run, the low-temperature κ(T) curves were measured upon heating from -192°C to 0°C. These measurements are explained in greater detail below.

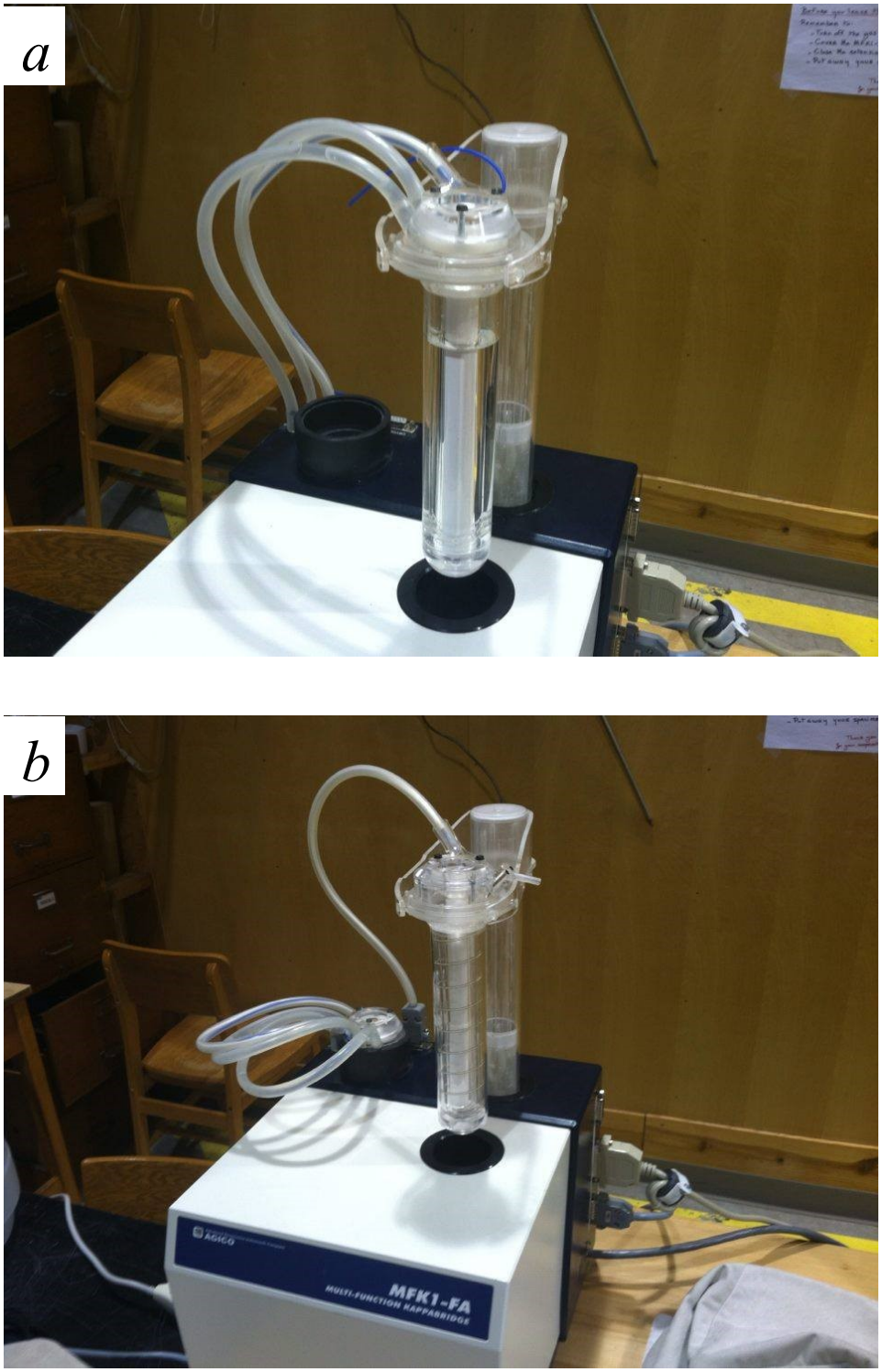

Figure 12: The AGICO MFK1-FA Kappabridge with a) a CS-3 Furnace Apparatus and b) a CS-L Cryostat used for thermomagnetic analyses.

For a thermomagnetic analysis, approximately 300-500 mg of powdered sample material was placed in a specialized quartz tube holder (Figure 13) together with a thermocouple to monitor the specimen's temperature during the measurement. For the initial low-temperature κ(T) curve measurement, the holder with specimen was inserted into the Cryostat and the entire apparatus was cooled to ~-192°C by slowly pouring liquid nitrogen into the Cryostat. Once the lowest temperature was reached, any remaining liquid nitrogen was quickly removed from the cryostat by flushing the system with argon gas to minimize oxidation of the specimen. The magnetic susceptibility was then measured at approximately 3°C increments as the specimen temperature slowly increased to 0°C. The average duration of a low-temperature measurement was about one and a half hours (Figure 14).

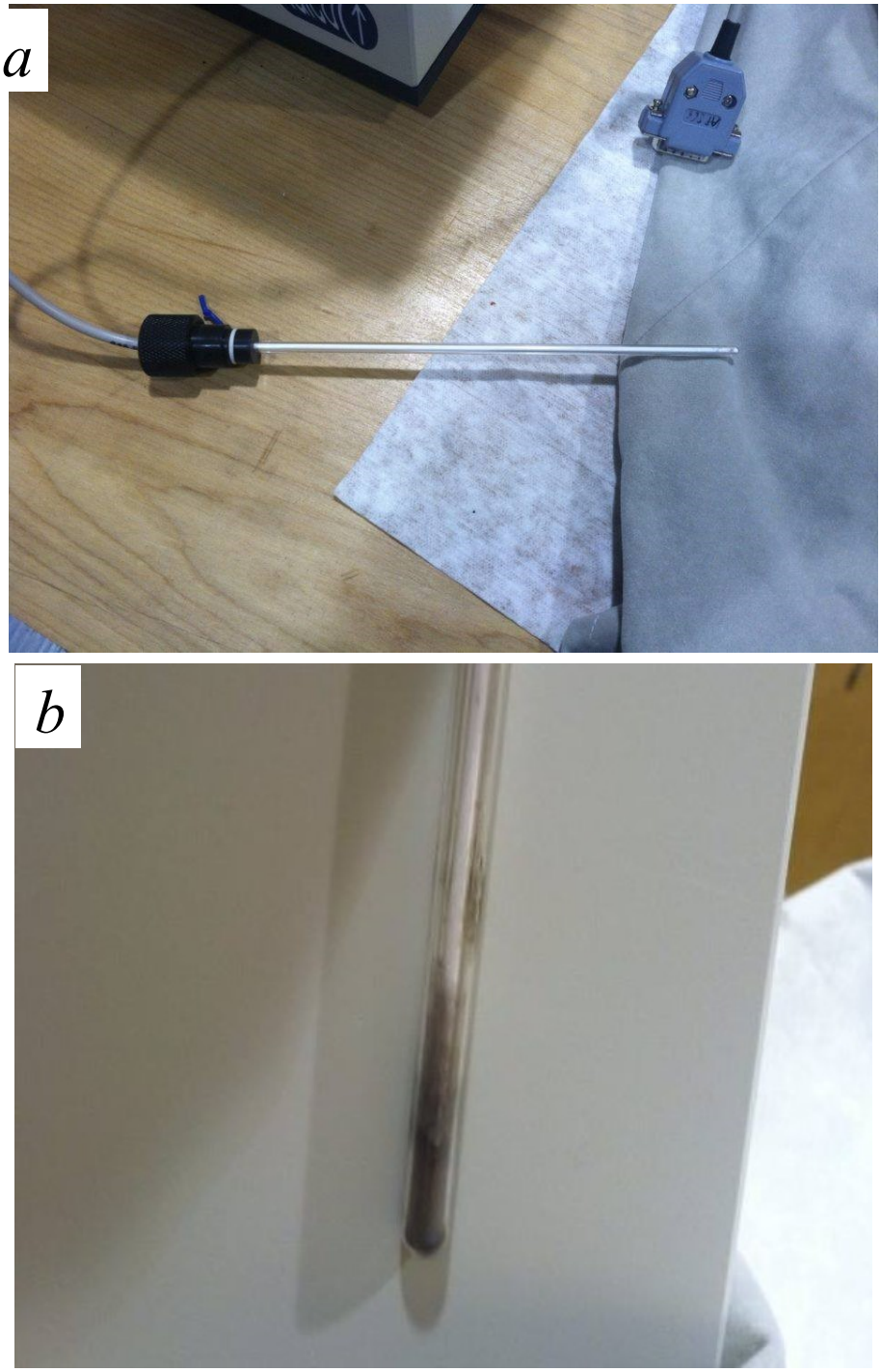

Figure 13: a) The temperature sensor (thermocouple) used to monitor the specimen's temperature during thermomagnetic measurements with the AGICO MFK1-FA Kappabridge. b) The quartz tube sample holder with specimen and thermocouple inserted.

Next, for the high-temperature κ(T) curve measurement, the tube holder with specimen and thermocouple was removed from the Cryostat and inserted into the Furnace. Special care was taken during the transfer not to move or disturb the specimen in the tube holder. The measurements of κ(T) were taken at approximately 5°C increments during thermal cycling between ~40°C and ~700°C (Figure 14) in an argon gas environment to prevent oxidation of the specimen. For a few selected samples, the high-temperature κ(T) curves were also measured in air to test whether oxidation causes change in the specimen. The average duration of a high-temperature measurement was about two hours.

After the high-temperature run, the holder assembly was again transferred back to the Cryostat and the second low-temperature κ(T) curve was measured (Figure 14) following the same procedure as for the initial low-temperature run. After all three κ(T) runs were measured, the specimen was removed from the quartz tube holder, and the tube and thermocouple were cleaned with isopropanol to prepare for the next specimen measurement.

The obtained LT and HT thermomagnetic curves were corrected for the empty Cryostat and Furnace signals, respectively, using the Cureval 8.0.2 program provided by AGICO (Chadima and Hrouda, 2012). The produced thermomagnetic curves allow for identification of magnetic minerals based on the Curie temperature analyses (e.g. ~585 °C for magnetite, ~680 °C for hematite) and also on the presence of low-temperature mineralogical transitions for magnetite (the Verwey transition at ~-153 °C; Verwey, 1939) and hematite (the Morin transition at ~-15 °C; Morin, 1950) (e.g., Figure 14).

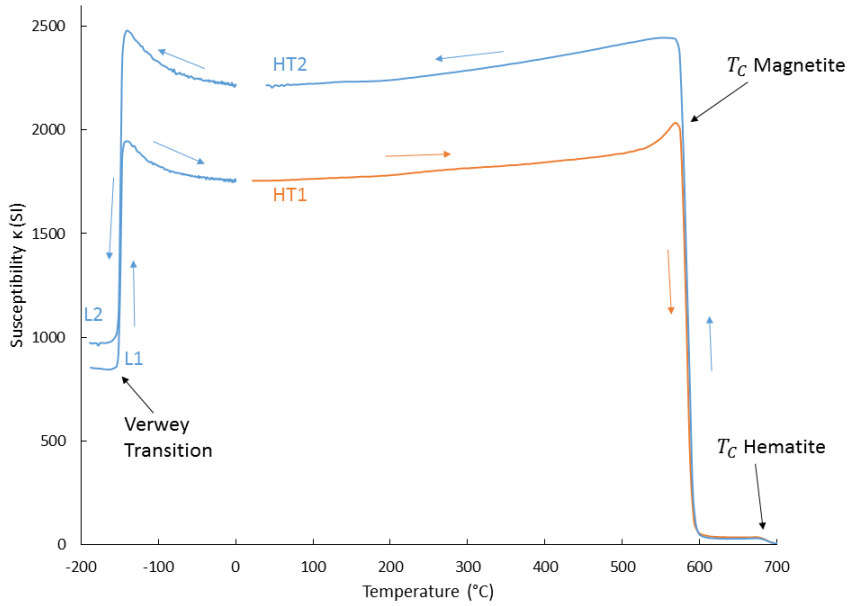

Figure 14: A typical dependence of low-field magnetic susceptibility (κ) versus temperature. The measurement starts with a low-temperature run L1 followed by a high-temperature run (HT1 – heating and HT2 - cooling) and second low-temperature run L2. The arrows show the direction of temperature change during each run. The sample exhibit a strong Verwey transition (VT) in both low-temperature runs indicating the presence of nearly stoichiometric magnetite. The presence of magnetite and hematite is also evidenced by the expressed drops in κ at the Curie temperatures of both magnetic minerals.

3.4 Anisotropy of Magnetic Susceptibility (AMS) and Bulk Magnetic Susceptibility

The measurement of anisotropy of magnetic susceptibility (AMS) consists in applying a magnetic field to a specimen and measurement of the induced magnetization in several different directions. In this project, the AMS was measured on cubic specimens with volume of 5 cm^3 using the AGICO MFK1-FA Kappabridge with an automatic rotating holder (Figure 15a). A 200 A/m magnetic field was applied in 3 directions and the corresponding susceptibility values (K) were measured. The same measurement sequence also provided the value of specimen's bulk low-field magnetic susceptibility.

The magnetic susceptibility measurements were also used to approximate an ellipsoid (the AMS ellipsoid as seen in figure 15b) with three principal axes K_1, K_2, and K_3 ($K_1 > K_2 > K_3$). The maximum (K_1) and minimum (K_3) axes of the AMS ellipsoid correspond to the greatest and weakest intensity of magnetization (and, hence, susceptibility value), respectively (Tarling and Hrouda, 1993).

With the knowledge of the components of the AMS ellipsoid, the mean bulk susceptibility:

$$K_m = (K_1 + K_2 + K_3)/3 \qquad (1)$$

the normalized magnetic foliation strength:

$$F = (K_2 - K_3)/K_m \quad (2)$$

and normalized magnetic lineation strength:

$$L = \frac{K_1 - K_2}{K_m} \qquad (3)$$

can be calculated. The magnetic foliation and lineation strength are used to ascertain the specimen's AMS relationship to the bedding of the member. Furthermore, the corrected degree of magnetic anisotropy (*Pj*):

$$Pj \quad = exp\sqrt{\{2[(n_1 - n_m)^2} + (n_2 - n_m)^2 + (n_3 - n_m)^2]\} \qquad (4)$$

and the shape parameter (*T*):

$$T = (2n_2 - n_1 - n_3)/(n_1 - n_3) \qquad (5)$$

can be derived where $n_1 = \ln K_1$, $n_2 = \ln K_2$, and $n_3 = \ln K_3$. The degree of magnetic anisotropy *Pj* measures the eccentricity of the AMS ellipsoid, or, in other words, how anisotropic the specimen is. The shape parameter defines the AMS ellipsoids shape that continuously varies from oblate (a disk-like) to prolate (a rod-like). AMS analysis was done using AGICO Anisoft 4.2 software.

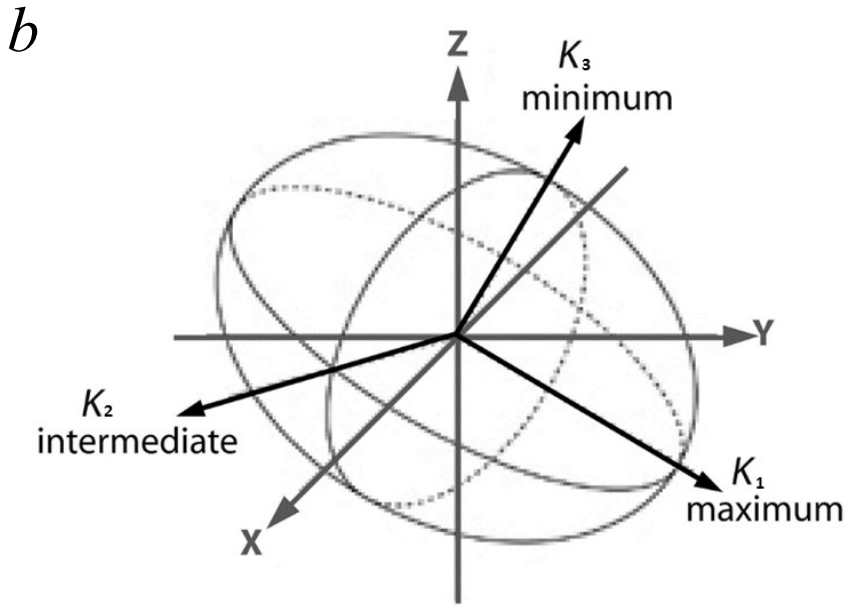

Figure 15: a) The AGICO MFK1-FA Kappabridge with an automatic rotating sample holder used for anisotropy of magnetic susceptibility (AMS) measurement. b) AMS Ellipsoid. K_1, K_2, and K_3 are the maximum, intermediate, and minimum axes (see text).

3.5 Königsberger ratio

The bulk susceptibility values (κ), derived during AMS measurements (K_m), were used to calculate the induced magnetization (J_i) described by the following general formula:

$$J_i = \kappa H \quad (6)$$

where H is the ambient magnetic field intensity (provided by the International Geomagnetic Reference Field (IGRF (www.ngdc.noaa.gov/geomag-web/))). The value of J_i together with the value of NRM (J_{NRM}) was used to calculate the Königsberger ratio (Q):

$$Q = \frac{J_{NRM}}{J_i} = \frac{J_{NRM}}{\kappa H} \quad (7)$$

which characterizes the relative contribution of induced and remanent magnetizations to the observed magnetic anomaly. $Q >> 1$ and $Q << 1$ correspond to the dominance of J_{NRM} or J_i, respectively, and $Q \approx 1$ represents a more complex case when the magnetizations are nearly equal.

3.6 Magnetic Hysteresis Analyses

Magnetic hysteresis measurements are useful for evaluating the magnetic domain state and grain-size distribution as well as for identification of different magnetic mineral phases in a sample. Magnetic hysteresis properties were measured with a MicroMag Model 2900 Alternating Gradient Magnetometer (AGM) housed in Michigan Tech's Earth Magnetism Laboratory (Figure 16a). An AGM allows measurement of both induced and remanent magnetic moments imparted in a specimen by an applied magnetic field as a function of the field strength (Graham, 2000).

For measurement, a small specimen (rock chip) is attached to the AGM sample holder stage (~3 x 3 mm^2 in size) using a small amount of diamagnetic silicone grease (Dow Release Compound 7) as adhesive (Figure 16b). After, the specimen is placed

between the poles of a water-cooled electromagnet capable of creating magnetic fields within a ±1.4 T range. The strength of the applied field is measured by a built-in Hall probe. The instrument uses two additional gradient field coils that create a periodically varying gradient magnetic field in the specimen region to induce specimen's vibration (Figure 16c). The vibration amplitude, measured by a piezoelectric transducer, is proportional to the specimen's magnetic moment.

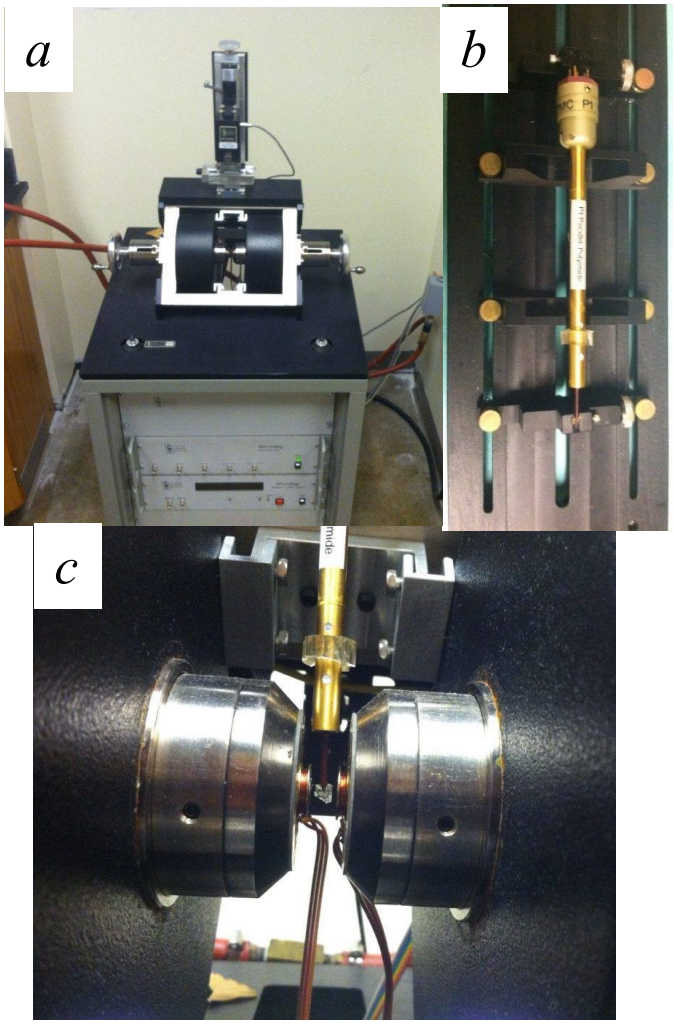

Figure 16: a) The MicroMag Model 2900 Alternating Gradient Magnetometer (AGM) used for magnetic hysteresis and FORC measurements. b) An AGM sample holder. c) The AGM measurement region with the specimen placed between the electromagnet poles.

Before each measurement, the sample holder stage was cleaned with isopropanol to remove any possible contaminants. The AGM was calibrated once a day (after the instrument was turned on) using an yttrium iron garnet sphere standard with a magnetic moment of 77.64 μAm. Following the calibration procedure, an empty probe measurement was taken for background signal removal.

The experimental protocol for magnetic hysteresis measurements consisted of three sequences. During the first sequence, the induced magnetic moment (M) of a specimen was measured as a function of the applied magnetic field (H). The applied field range varied between ±1.2 T and ±1.4 T (with the respective field increments of 12 mT and 14 mT) depending on the sample characteristics. The orientation of the chips on the AGM probe was kept consistent to reduce any effects from magnetic anisotropy due to chip orientation. After the measurement was completed, the specialized AGM software was used to subtract the empty probe signal from the raw data and to apply an additional correction to remove the diamagnetic and paramagnetic signals. The adjusted M(H) curve (a hysteresis loop) defined three magnetic hysteresis parameters - the saturation magnetization (M_s), saturation remanent magnetization (M_{rs}), and coercive force (H_c) (Figure 16).

The second sequence consisted in measuring the DC (backfield) demagnetization of a saturation remanent magnetization (M_{rs}). First, a strong magnetic field of the same maximum strength used in the hysteresis (1.2 T or 1.4 T) was applied in one direction to impart M_{rs}. Then, a small field (H_r) sweep was applied in the opposite direction, demagnetizing a small fraction of M_{rs}. After the field H_r was switched off, the specimen's remaining magnetic remanence, M_r, was measured. This process was repeated using the incrementally increasing H_r field (with 50 mT or 100 mT increments) until the maximum field strength (1.2 T or 1.4 T) was reached (Figure 16). The obtained DC demagnetization curve, $M_r(H_r)$, was then used to estimate the fourth hysteresis parameter – the coercivity of remanence, H_{cr} (a reverse magnetic field required to reduce M_{rs} to zero) (Figure 17).

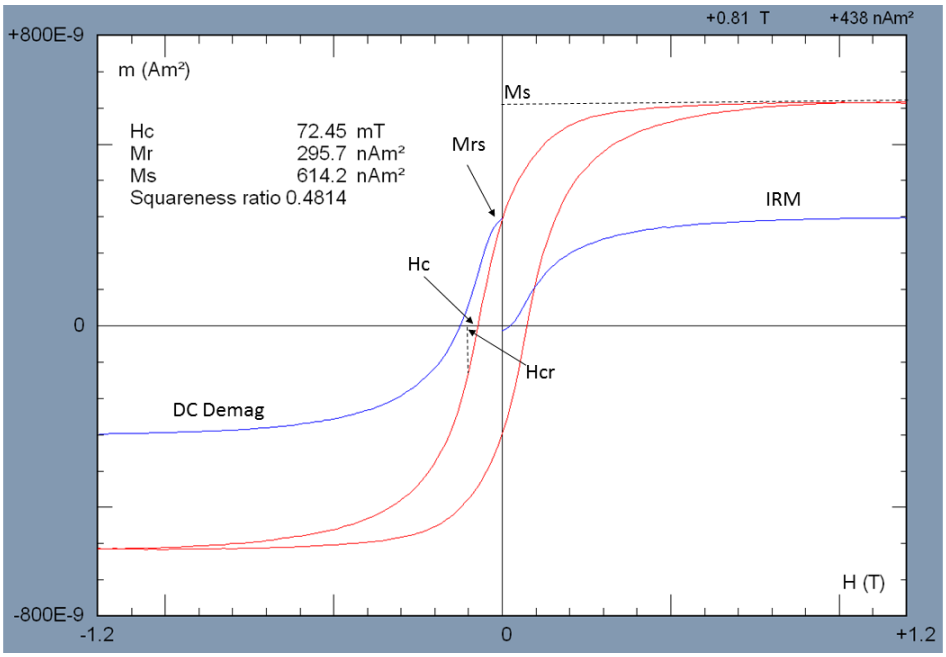

Figure 17: A typical magnetic hysteresis plot. H: Applied Magnetic field; M: Induced Magnetization; Ms: Saturation Magnetization; Mrs: Remanent Saturation Magnetization; Hc: Coercive Force (Coercivity); Hcr: Coercivity of Remanence; IRM: Isothermal Remanent Magnetization; DC Demag: DC Demagnetization Remanence; Red line: magnetic hysteresis loop.

After the DC demagnetization step, the sample was demagnetized (via alternating field demagnetization) in preparation for the third sequence, acquisition of the isothermal remanent magnetization (IRM) curve. Once the sample was completely demagnetized, a small field (H) was applied to the specimen to induce remanence (M_r), which was measured. This process was continued with increasingly strong fields (H) until the specimens' saturation remanence (M_{rs}) was reached. The IRM curve was used to estimate the saturation field level (H_s) and to obtain insight into the presence of magnetically hard magnetic minerals (indicated by an inflection and/or non-saturation of the IRM curve).

In addition to visual analysis of the shape of the measured hysteresis loops, IRM, and backfield demagnetization curves, the M_{rs}/M_s ratios were plotted versus the H_{cr}/H_c ratios on a Day plot (Day et al., 1977). The Day plot is a conventional means to characterize

the magnetic domain state: single domain (SD), pseudo-single domain (PSD), or multi-domain (MD).

3.7 First-Order Reversal Curve (FORC) diagram

In addition to the conventional magnetic hysteresis measurements described in the previous section, a first-order reversal curve (FORC) analyses (e.g., Mayergoyz, 1986) were performed. The FORC technique is more sensitive to subtle variations in hysteresis properties than bulk hysteresis parameters and allows to better resolve signals from different magnetic phases (e.g., Pike et al., 1999; Roberts et al., 2000). Measurement of a FORC dataset begins by saturating a sample in a large positive magnetic field. The field is then decreased to a set intensity in the reversed direction (H_a). An applied field (H_b) is then applied increasing from H_a back to saturation during which a partial hysteresis curve (a first-order reversal curve) is recorded (Figure 18a). Then the cycle is repeated for a number of H_a values to obtain a set of FORCs (Figure 18b).

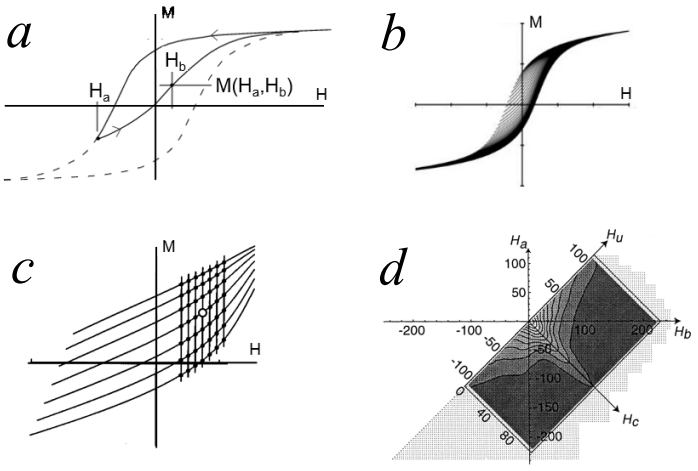

Figure 18: a) Definition of a first-order reversal curve (FORC). b) An example of a full set of FORCs. c) A subset of seven consecutive FORCs with the points representing a 7x7 local grid array (SF = 3) of evenly spaced data points in both H_a and H_b. The open circle shows the central point to which the smoothed values of $M(H_a,H_b)$ is assigned. d) An example of a continuous FORC distribution plot in the $\{H_a,H_b\}$ and $\{H_c,H_u\}$ coordinates (see text). When the latter coordinate axes are used, the plot is called a FORC diagram.

The magnetic moment at the applied field H_b on the FORC with reversal point H_a is denoted by $M(H_a,H_b)$, where $H_a > H_b$. The FORC distribution density at a point (H_a, H_b) is defined as the mixed second derivative (Pike et al., 1999):

$$\rho(H_a, H_b) \equiv -\partial^2 M(H_a, H_b)/\partial H_a \partial H_b. \qquad (7)$$

The value of $M(H_a,H_b)$ at a point P is calculated by fitting a polynomial surface $a_1+a_2H_a+a_3H_a^2+a_4H_b+a_5H_b^2+a_6H_aH_b$ on a local square grid centered at the point P (Figure 18c) . The value a_6 represents $\rho(H_a,H_b)$ at point P. The smoothing factor (SF) defines the number of points $(2SF + 1)^2$ on the local grid used for the fitting. The SF can vary from 1 (no smoothing) to 8 for samples with a low signal-to-noise ratio (e.g., Roberts et al., 2000). The final step in creating a FORC diagram involves rotating the FORC distribution coordinates $\{H_a, H_b\}$ by 45° to:

$$H_{c\prime} = (H_b - H_a)/2 \quad (8)$$

$$H_u = (H_b + H_a)/2 \quad (9)$$

A contour plot is then created with $H_u$and $H_{c\prime}$ on the vertical and horizontal axes, respectively (Roberts et al., 2000) (Figure 18d).

For this project, the measurement of first-order reversal curves was conducted using the AGM (described in the previous section) from the same specimens (rock chips) that were used for magnetic hysteresis loop, DC demagnetization, and IRM measurements. Measurement of a FORC dataset (which typically contains more than a hundred curves) can be quite lengthy (5-6 hours per specimen) so that this is extremely important that the measurement parameters are specified correctly. In order to find the most suitable parameters for each specimen, a dump (low-resolution) FORC (~1 hour measurement time) was measured first using a trial set of parameters (typically, based on the bulk hysteresis loop inspection). The dump FORC data were processed and, if needed, the parameters were adjusted and used to measure a high-resolution FORC set. The FORC data processing and plotting was done using the FORCinel v.3.0 software (Harrison and Feinberg, 2008).

3.8 Scanning Electron Microscopy (SEM)

The opaque mineralogy of five selected samples was analyzed using a FEI Philips XL 40 Environmental Scanning Electron Microscope (ESEM) with an energy dispersive spectrometry (EDS) system (Figure 19). The samples were cut from selected cores and block samples and prepared at the MTU Rock Preparation laboratory. Each specimen was polished on one side using increasing grades of diamond coated grinding disk down to approximately 0.5 micron. Care was taken to make sure that the specimen was not scratched. Prior to ESEM work, all samples were coated in carbon to preclude electrical charge accumulation on their surface.

Figure 19: Philips XL40 ESEM at MTU used for electron microscopy analyses.

All specimens were observed with an initial working distance of 10 mm and accelerating voltage of 15 kV, which is optimal for excitation of the Fe K shell. Some specimens were observed at 30 kV when an increased magnification was used. Backscattered electron imaging was used to identify potential iron oxide grains. The composition of the oxide grains was determined by means of energy dispersive spectrometry.

4. Results

4.1 General description of samples

A visual examination of the samples of the Traders Member shows characteristic BIF banding composed of three distinct bands of material; a grey to dark grey band, a rust red to bright red band, and a white band (Figure 20). The grey and red bands appear dominant and the white bands are sparse. The darker sections consist of grey to dark grey bands ranging in size from as small as 1 mm to as thick as 2 cm. The dark layers have a metallic shimmer that is easily noticeable if a light is shined upon the rock. Grain size is very fine in appearance for the dark section. The red and white bands appear to have a less fine grain size and do not have a metallic shimmer. Their width is consistent with the dark layers. Some samples have calcite or quartz veins.

Figure 20: Examples of Traders Member samples exhibiting alternating layers of iron and non-iron layers. a) FR02A b) FR02B

The Curry Member samples do not exhibit the characteristic banding associated with BIF. The banding that does exist in the samples is sparse and consists of alternating white and grey layers. The samples from the Site LH appear to have a some banding, but not to the extent characteristic of BIF (Figure 21a). The red layers usually associated with BIF are not as frequent in the Curry Member samples as one would expect for a BIF (Figure 21b). The dominant layer is a grey to dark grey band that ranges in width from 1 mm to the entire sample, is very fine grained and has a metallic shimmer. The white and red layers range in size from 1 mm to 1 cm and have a very fine to fine grain structure. Quartz and calcite veins are common throughout. Some Curry samples have a dull appearance. For site CF0, regular banding is revealed when the samples were cut, although there appears to be little difference between the layers (Figure 21a). Site CF1 samples, when cut, do not reveal regular banding. A metallic shimmer is present, although it is faint (Figure 21b).

Figure 21: Examples of Curry Member samples exhibiting alternating layers of iron and non-iron layers. a) LH02 b) CF12

4.2 Natural Remanent Magnetization (NRM)

The (NRM) of the Traders Member were measured from six independently oriented samples from Site FR01 (one specimen per sample) and four independently oriented samples from Site FR02 (two specimens per sample). The NRM values ranged between 0.64 and 5.55 A/m with the mean of 2.96 ± 1.61 (1 σ) A/m and the median at 3.30 A/m. An additional sample (FR01E) representing the thin slate layer cutting the Traders Member outcrop yielded a much weaker value of NRM of $1.96*10^{-3}$ A/m (Table 1).

The NRM values of the Curry Member was measured from two independently oriented samples from Site LH (two specimen per sample), four independently oriented samples from Site CF0 (six specimens), and two independently oriented samples from Site CF1 (two specimens per sample). The NRM values for Site CF0 ranged from $8.99*10^{-3}$ A/m to 0.81 A/m with the mean of 0.292 ± 0.284 (1 σ) A/m and the median at 0.19 A/m. The specimens from Sites CF1 and LH yielded very different NRM values. Site CF1 had NRM values ranging from of 0.09 μT to 3.97 A/m with a mean of 2.56 ± 1.53 (1 σ) A/m and a median at 3.09 A/m. Site LH had NRM values ranging from of 0.559 A/m to 2.28 A/m with a mean of 1.61 ± 0.691 (1 σ) A/m and a median at 1.79 A/m (Table 1).

A comparison of the Koenigsberger ratio (Q) for specimens of the Traders Member and Curry Member shows a considerable scatter of Q values (Figure 22). All Q values show a combination of induced and remanent magnetization (Q≈1), the Traders Member specimens appear to have higher Q ratios (with exception of FR01E) whereas Curry Member specimens appear to have lower Q ratios (specimens from sample CF12 are exceptions). However, a distinct trend cannot be ascertained from the measured Q ratios.

Table 1: Summary of paleomagnetic data from Curry and Traders Members. Declination and Inclination are paleomagnetic declination and inclination corrected for structural tilt. n is amount of TRM steps

Name	Declination (°)	Inclination (°)	n
CF01A	59.1	-12.4	38
CF03A	85.5	-0.2	34
CF03B	133.2	39.8	38
CF04A	331.8	-8.2	39
CF04B	326.8	-8.3	38
CF05A	327.8	16	38
CF11A	222.2	25.3	36
CF12A	199.9	16.7	37
CF12B	204.6	25.5	36
Mean	210.1	10.5	
FR01A	230.9	60.7	36
FR01B	224.1	34.2	39
FR01C	241.1	44.2	38
FR01D	249.8	31.6	38
FR01E	89.9	40.5	37
FR01F	8.2	51.0	39
FR01G	258.9	21.4	39
FR02A1	293.6	17.4	37
FR02A2	186.3	-34.3	38
FR02B1	294.3	43.2	37
FR02B2	123.1	50.8	37
FR02C2	90.1	-56.0	39
FR02C3	92.8	73.3	40
FR02D1	211.5	74.4	37
FR02D2	115.4	49.0	36
Mean	180.7	33.4	

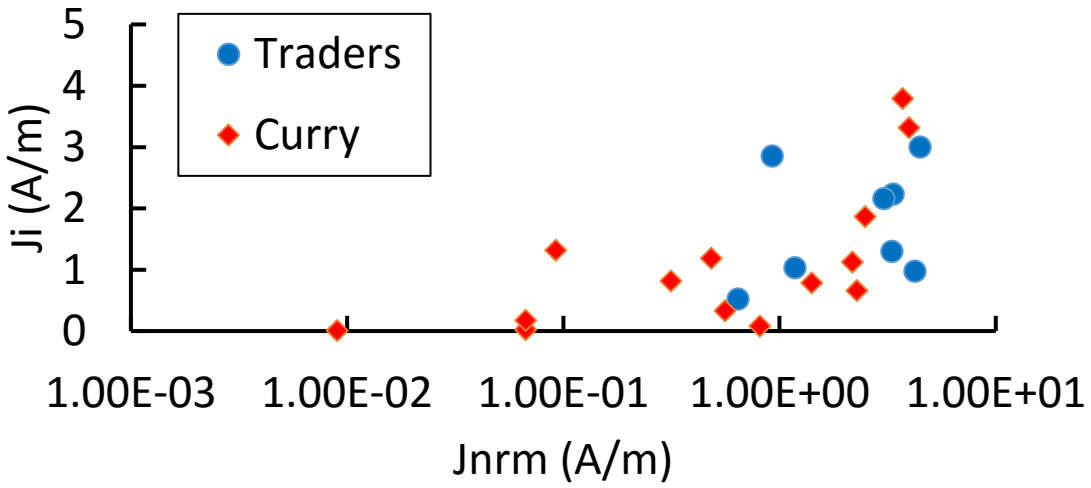

Figure 22: Plot of the Koenigsberger ratios (Q) for the Curry and Traders Members comparing remanent magnetization (J_{nrm}) to induced magnetization (J_i). FR01E not shown.

The initial low-temperature demagnetization (LTD) resulted in demagnetization of 25% to 85% of the original NRM for the Traders Member specimens (in average above >70%) (Figure 23). For the Curry Member specimens from Site CF0 were less affected by LTD – between 15% and 50% (Figure 23), whereas the specimens from Site CF1 lost from 65% to 91% of the original NRM. These results indicate a higher relative content of nearly stoichiometric magnetite in the Traders Member specimens and in the Site CF specimens.

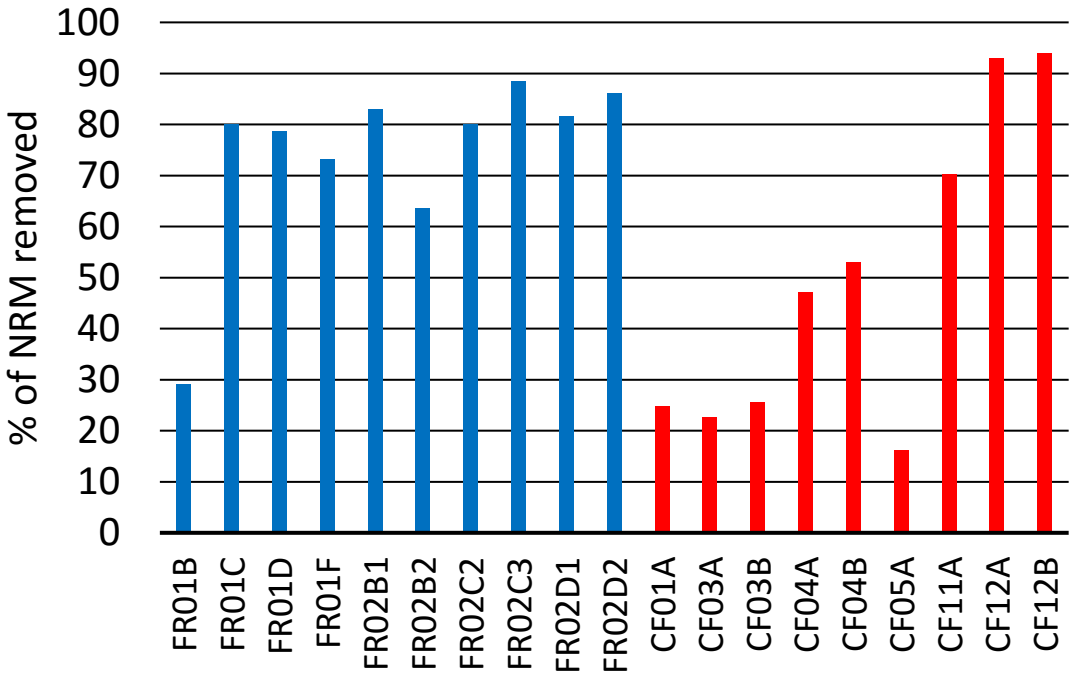

Figure 23: Bar graph showing the percentage of Natural Remanent Magnetization (NRM) removed by low-temperature demagnetization for the Traders and Curry Members.

After thermal demagnetization at 600°C, seven out of ten Traders Member specimens lost more than 90% of their original NRM which is consistent with passing the magnetite Curie temperature (Figure 24). For the Curry Member, only specimens from sample CF12 had lost more the 95% of original NRM (Figure 24). The rest of the Curry Member specimens retained between 55% to 80% of their original NRM, meaning that a mineral with a greater Curie temperature is holding a large fraction of the NRM, such as hematite.

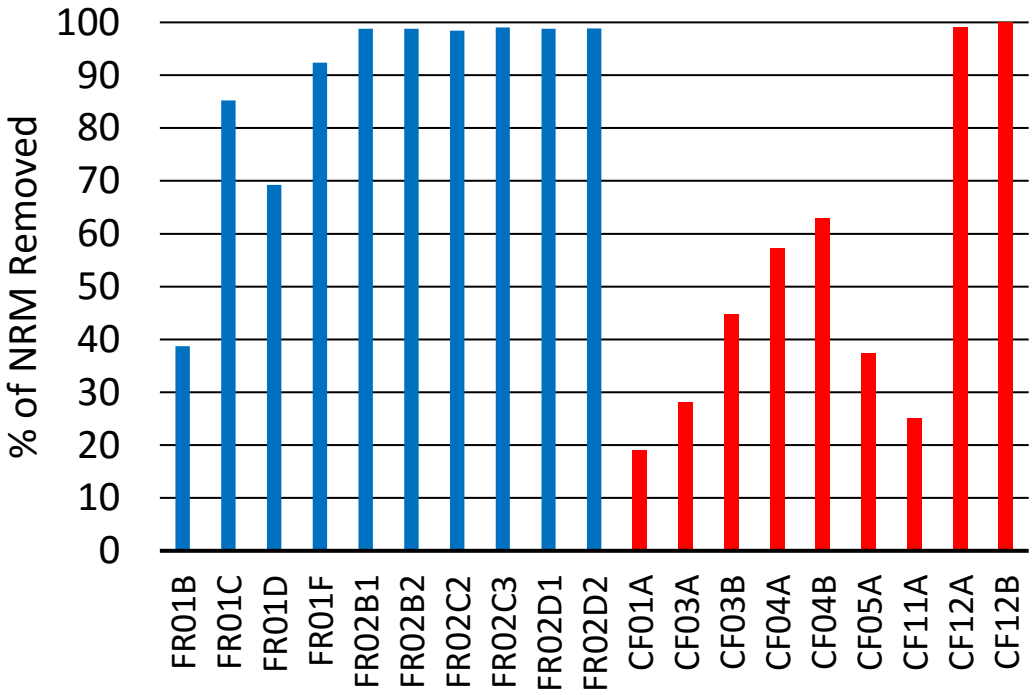

Figure 24: Bar graph showing the percentage of Natural Remanent Magnetization (NRM) removed by 600°C for the Traders and Curry Members.

Approximately half of the Traders Member specimens manifested a single low-coercivity/temperature NRM component (Figure 25). The characteristic remanent magnetization (ChRM) plots to the southwest and has an upward inclination (Figure 26). Specimens from Curry Member Site CF1 plot similar to those of the Traders Member. Five of the specimens failed to yield acceptable paleomagnetic data.

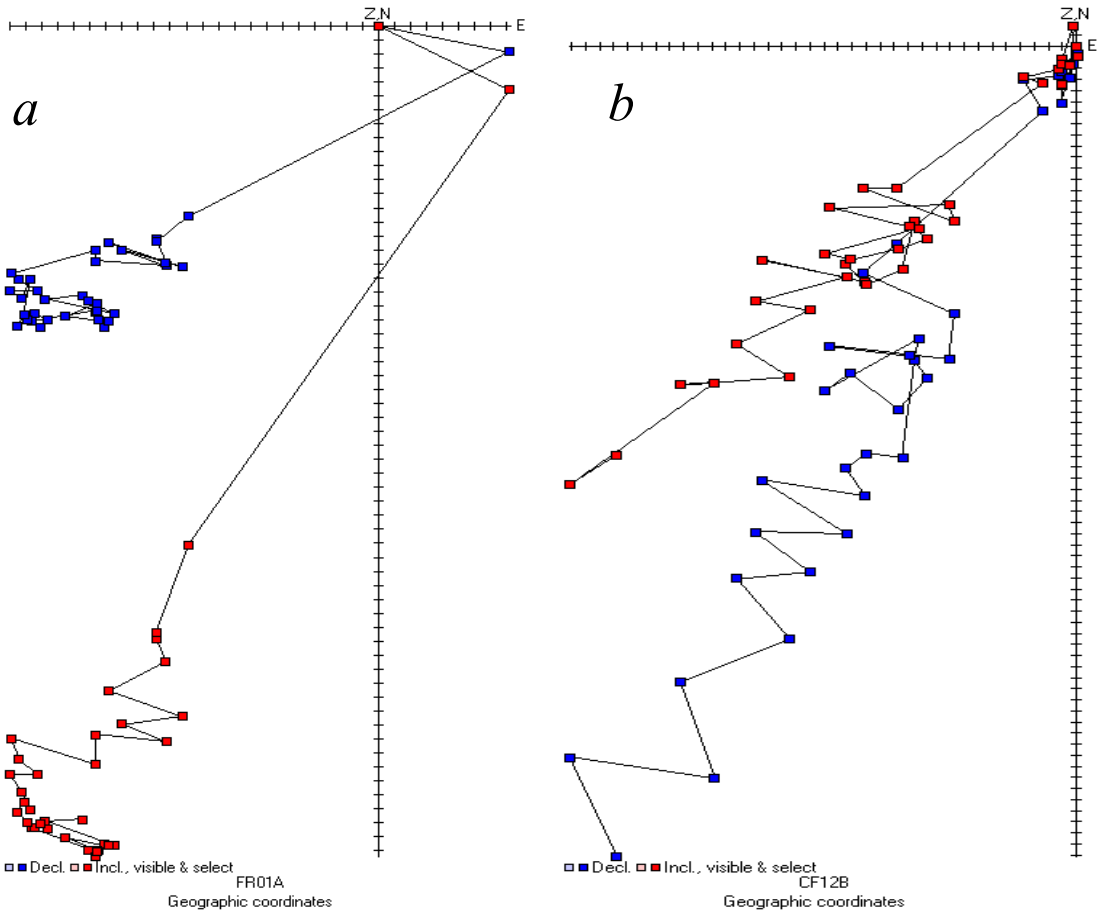

Figure 25: Examples of vector endpoint diagrams for the Traders and Curry Members. a) FR01A, b) CF12B. Blue symbols represent data point projections on vertical plane; red symbols represent data point projections on the horizontal plane.

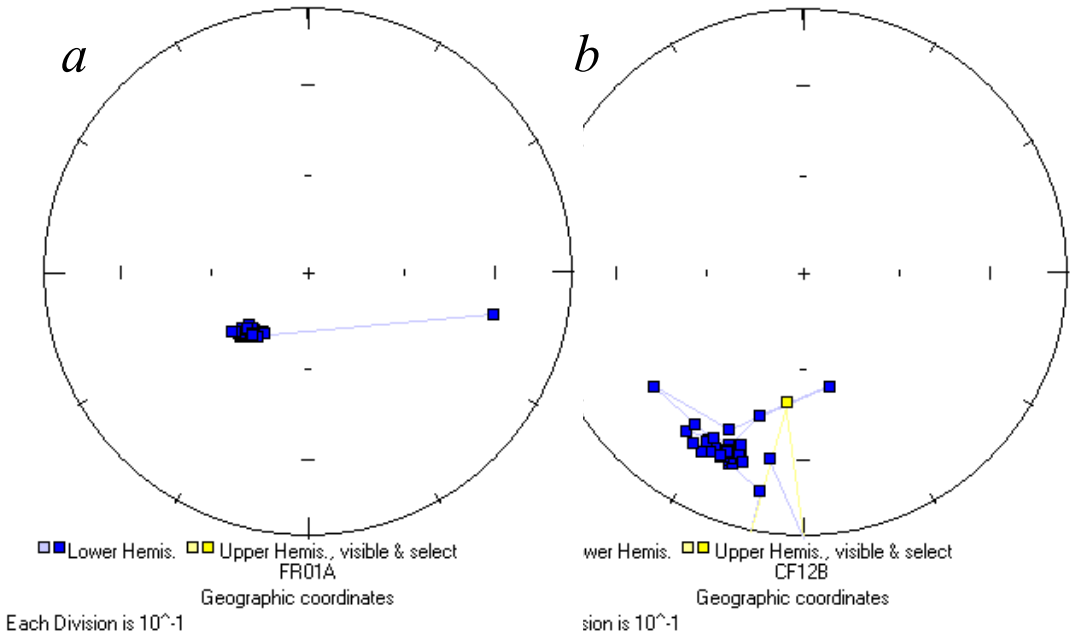

Figure 26: Examples of Equal Area plots for the Traders and Curry Members. a) FR01A, b) CF12B.

The Curry Member specimens manifested a single low-coercivity/temperature NRM component (Figure 27). The ChRM for the Curry Members plots with a low downward inclination and appears in both the northeast and northwest (Figure 28). Two of the specimens failed to yield acceptable paleomagnetic data.

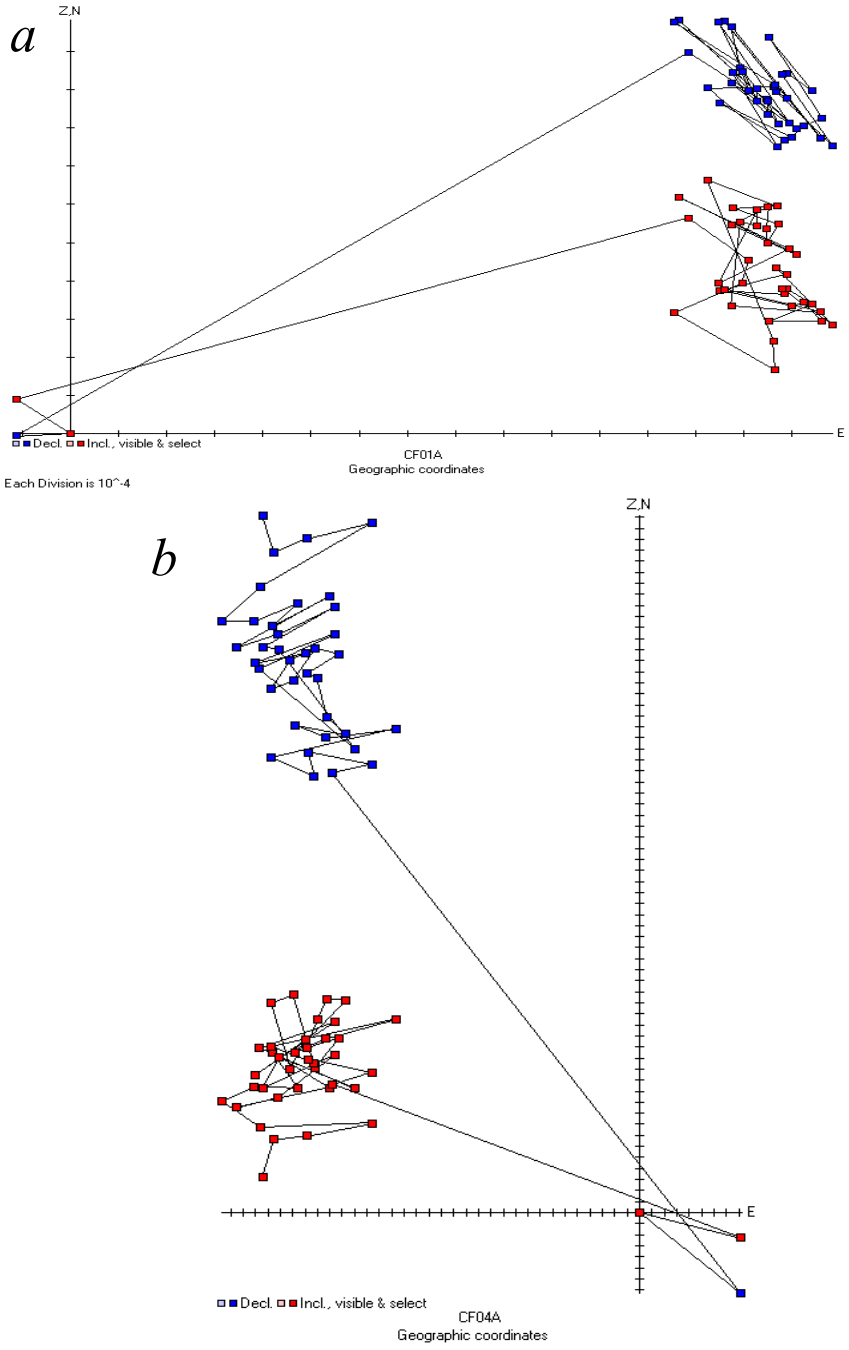

Figure 27: Examples of vector endpoint diagrams for the Curry Member. a) CF01A, b) CF04A. Blue symbols represent data point projections on vertical plane; red symbols represent data point projections on the horizontal plane.

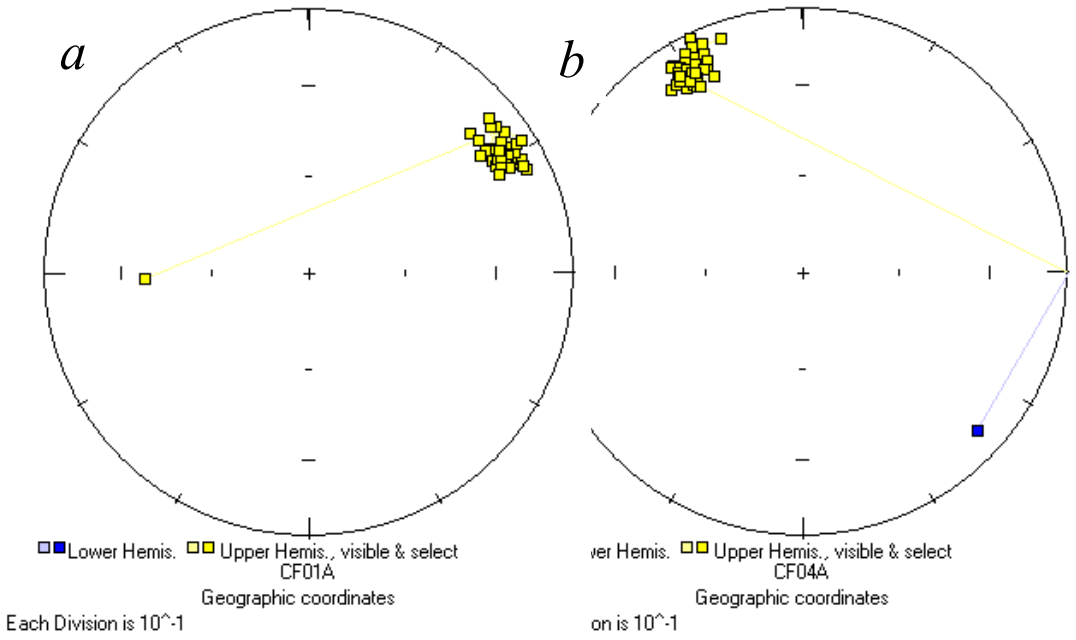

Figure 28: Examples of equal area plots for the Curry Member. a) CF01A, b) CF04A.

4.3 Thermomagnetic Analyses of Low-Field Susceptibility

Thermomagnetic analyses were conducted on ten samples from the Traders Member sites FR01 and FR02 (Figure 29 and 30). Nine samples represented the iron-formation and one sample (FR01E) represented a thin ferruginous slate layer cutting through the outcrop between the sites. The κ(T) curves for all nine iron-bearing samples showed the presence of a ferromagnetic mineral phase with the Curie temperature about 585-590°C consistent with magnetite as well as the characteristic susceptibility peaks near -153°C associated with the Verwey transition (Figure 29a-d, f; Figure 30a-d), indicating that this magnetite is nearly stoichiometric. Eight of the samples also showed the presence of an additional ferromagnetic mineral phase with the Curie temperature about 670-680°C (Figure 29a,b,d,f) which was interpreted as hematite.

All the κ(T) curves are irreversible. For eight samples (except for FR01D), the cooling curve of the high-temperature run showed an increase in susceptibility compared to the initial value indicating formation of a new magnetic mineral phase upon thermal

treatment (Figures 29d). The Curie temperature of this new phase is about 585-590°C which, together with more expressed Verwey transition peaks observed from second low-temperature runs, indicate that the newly formed phase is nearly stoichiometric magnetite. However, the "hematite" part of all the curves (between ~600 and 700°C) is reversible or nearly reversible indicating that the new magnetite is likely formed by heating-induced alteration of clays but not at the expense of hematite (by hematite reduction). Some samples also exhibit inflections at ~150-200°C on the cooling curves (for example, Figure 29a,b; 30a). These inflections likely reflect a difference in the superimposed κ(T) signals from the initially present and newly formed magnetite (due to their difference in magnetic domain state, internal stress, etc.) rather than the presence of an additional magnetic mineral phase.

Sample FR01D exhibited a different type of irreversibility – the cooling curve of the high-temperature run plots below the heating curve indicating a decrease in susceptibility. The sample also shows a broad maximum on the heating κ(T) curve between 200°C and 350°C which disappears from the cooling curve (Figure 29d). The strength of the Verwey transition measured before and after heating remains the same indicating the initially present magnetite is not affected by heating. In comparison to the other eight iron-bearing samples of the Traders Member, sample FR01D also lacks a Hopkinson peak on the heating κ(T) curve indicating the dominance of large, multi-domain magnetite grains (Dunlop, 1974). The cooling κ(T) curve, however, shows a weakly expressed Hopkinson peak. The observed irreversibility may reflect a heating-induced re-arrangement of magnetic domain structure (Kosterov and Prevot, 1998) rather than destruction of a magnetic mineral phase.

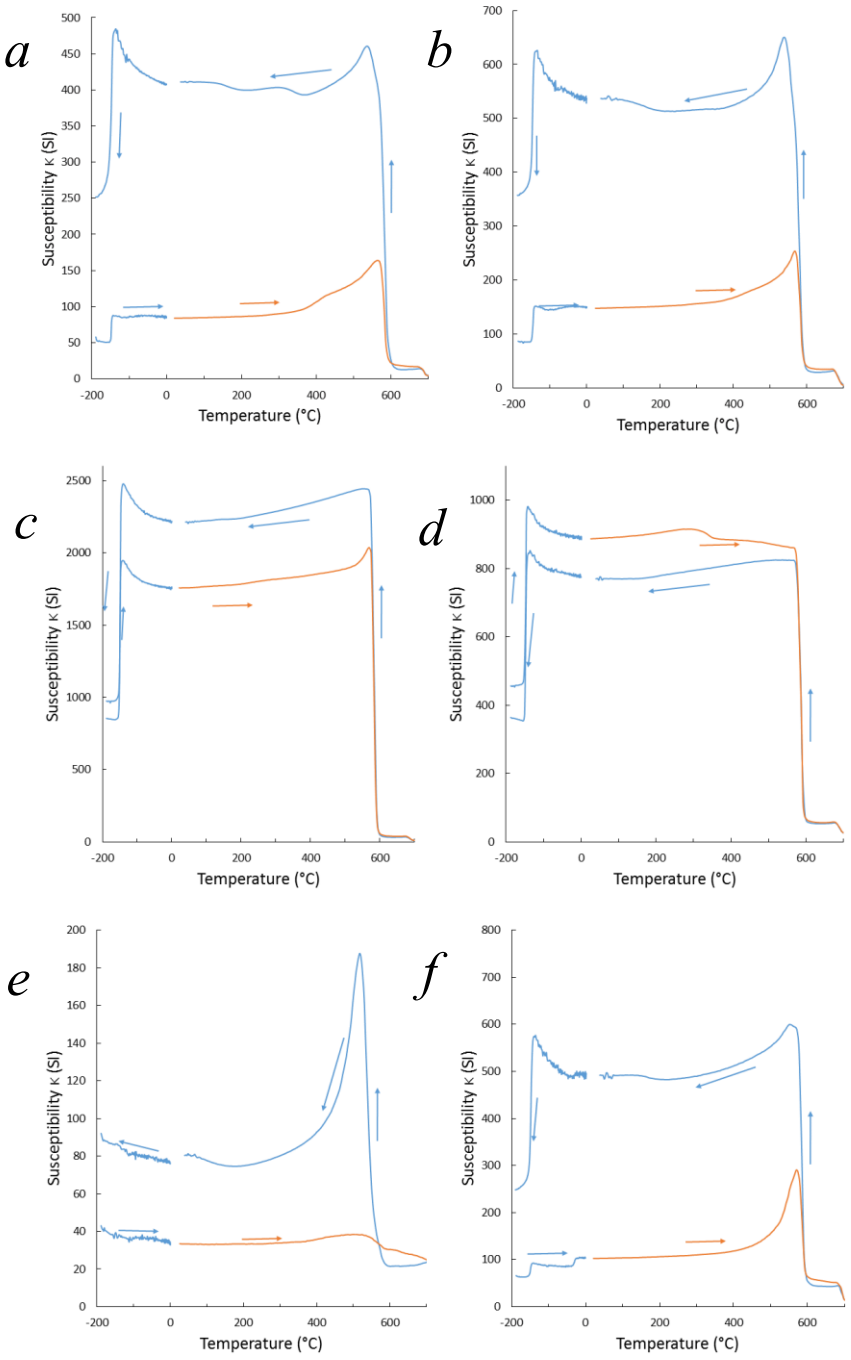

Figure 29: Dependence of low-field magnetic susceptibility (κ) versus temperature measured from the Traders Member samples: a) FR01A, b) FR01B, c) FR01C, d) FR01D, e) FR01E, and f) FR01F. The arrows show the direction of temperature change during high-temperature runs (heating or cooling).

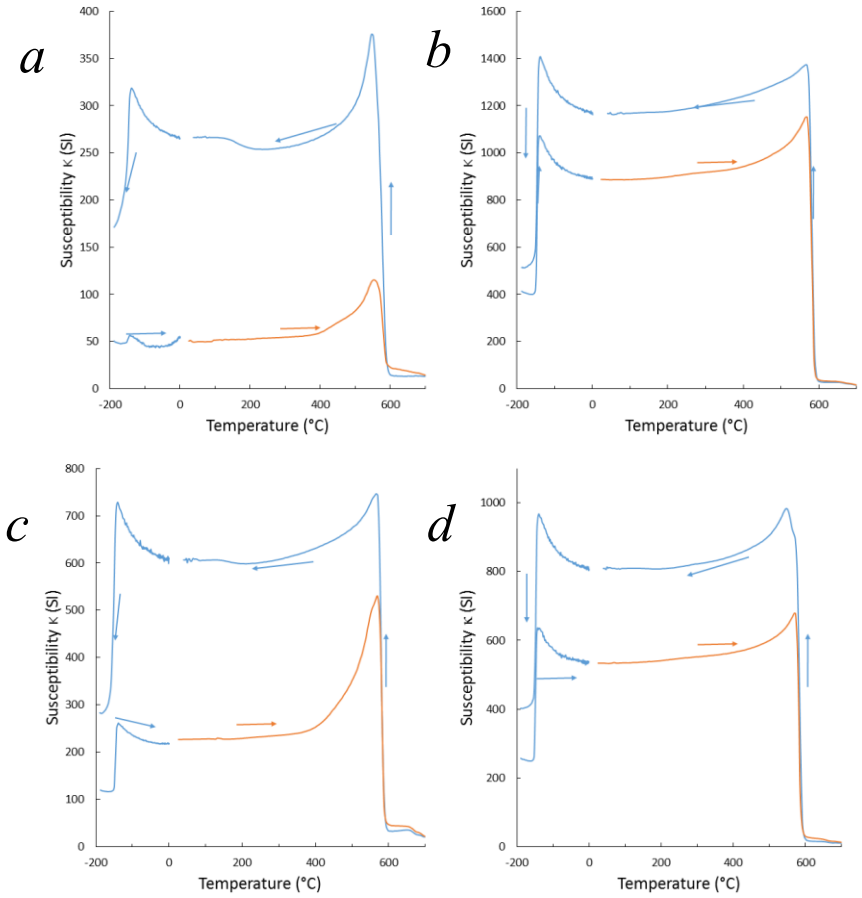

Figure 30: Dependence of low-field magnetic susceptibility (κ) versus temperature measured from the Traders Member samples: a) FR02A, b) FR02B, c) FR03C, and d) FR04D. The arrows show the direction of temperature change during high-temperature runs (heating or cooling).

Sample FR01E (ferruginous slate) was characterized by substantially lower magnetic susceptibility and showed no Verwey transition in the initial low-temperature κ(T) curve. The heating curve of the high-temperature run showed a broad low peak between ~380°C and 590°C and the presence of a magnetic phase with Curie temperature at ~680-690°C, most likely hematite. In contrast to the iron-formation samples, this hematite signal disappears from the cooling curve which is irreversible and indicates heating-induced formation of a new magnetic mineral phase with the Curie temperatures between ~540°C and 590°C. The strong Hopkinson peak observed from the cooling curve indicates that the phase is in single-domain magnetic state (Dunlop, 1974). No Verwey

transition was observed from the second low-temperature κ(T) curve. Therefore, the observed irreversibility for FR01E likely reflects reduction of hematite into a non-stoichiometric cation-deficient magnetite phase (e.g., Özdemir et al., 1993).

The samples of the Curry Member from Site LH exhibited thermomagnetic curves identical to those of most of the Traders Member (Figure 31). The initial low-temperature κ(T) curves indicate that both samples contain nearly stoichiometric magnetite. The Hopkinson peaks are stronger than for most of the FR01 and FR02 samples which indicates a more single-domain behavior implying a smaller grain-size of the magnetite grains. A strong irreversibility due to the neoformation of magnetite was also observed in both samples.

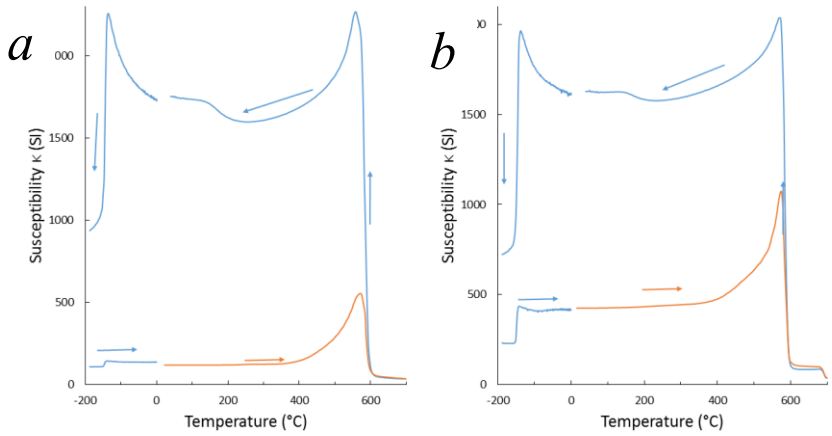

Figure 31: Dependence of low-field magnetic susceptibility (κ) versus temperature measured from the Curry Member samples: a) LH01 and b) LH02. The arrows show the direction of temperature change during high-temperature runs (heating or cooling).

Thermomagnetic behavior shown by the Curry Member samples from Site CF0 (Figure 32a-d) is more diverse than that of the FR and LH samples. While two samples (CF04 and CF05) exhibit κ(T) curves generally similar to that of the LH samples, the two other (CF01 and CF03) show no Verwey transition on the initial low-temperature κ(T) curves (Figure 32a,b). Most likely, CF01 and CF03 do not contain significant amounts of magnetite, but both contain hematite with the Curie temperature at ~680-690°C. The strong Hopkinson peaks observed from the heating curves at ~500-580°C most likely correspond to newly formed magnetite by heating. In addition, in contrast to most of the FR and LH

samples, all four CF0 samples exhibit irreversibility in the 600-700°C temperature interval (Figure 32a-d) most likely indicating the reduction of hematite into magnetite upon heating in argon. Note that this irreversibility for CF03 in Figure 32b is masked by a strong magnetite signal from the cooling curve. Most likely, the neoformation of magnetite in these samples occurs by both hematite reduction and clay conversion mechanisms.

The κ(T) curves measured from the Curry Member samples from Site CF1 indicate the presence of nearly-stoichiometric magnetite as well as hematite (Figure 32). Both samples also exhibit strongly irreversible behavior due to the neoformation of magnetite. The high-temperature κ(T) curves (>600°C) are only slightly irreversible so the magnetite primarily forms by heating-induced clay conversion and the reduction of hematite plays a minor role.

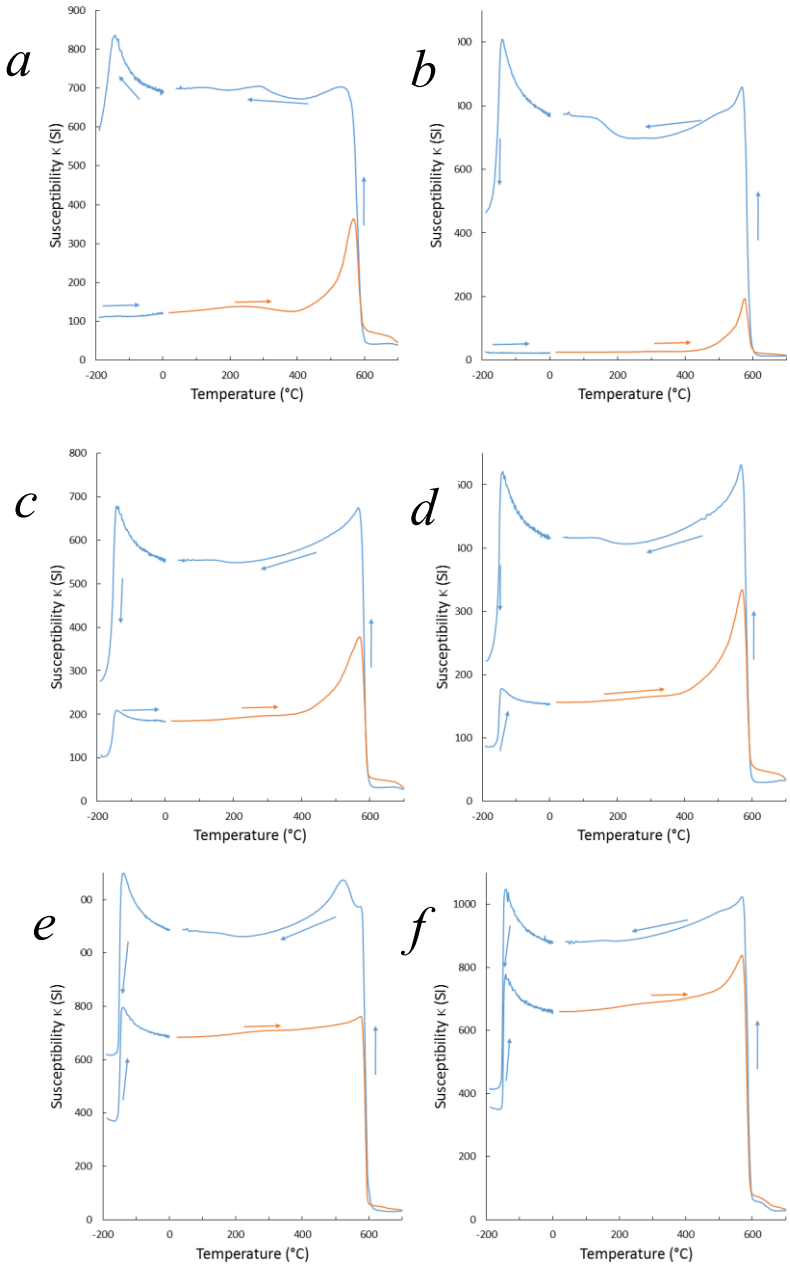

Figure 32: Dependence of low-field magnetic susceptibility (κ) versus temperature measured from the Curry Member samples: a) CF01, b) CF03, c) CF04, d) CF05, e) CF11, and f) CF12. The arrows show the direction of temperature change during high-temperature runs (heating or cooling).

4.4 Magnetic Hysteresis Analyses

The measured magnetic hysteresis loops showed a variety of loop shapes including regular, “wasp-waisted”, and “potbellied” loops (Figure 33). A regular hysteresis loop is widest when the induced magnetization is zero and narrows as the field approaches the saturation field. A wasp-waisted loop is one where the width of the curve narrows as the magnetization approaches zero then expands again when the reverse polarization is applied (Figure 33c). Potbellied loops, in contrast, expand as magnetization approaches zero then narrow for intermediate fields, and expand again as the field grows towards saturation (e.g. Figure 33a).

The magnetic hysteresis loops measured from the Traders Member samples exhibit mostly wasp-waisted and potbellied shape (Figure 33) consistent with a mixture of a low coercivity (magnetite) and high coercivity (hematite) magnetic mineral phases observed from the thermomagnetic data. The presence of the two mineral phases is also evident from the DC demagnetization and IRM curves many of which show an inflection point at ~0.1-0.2 T (corresponding to magnetite saturation). These curves do not saturate at the highest magnetic field applied (1.2-1.4 T), indicating the presence of magnetically hard phases such as hematite which would saturate in much higher fields (>5 T) (Figure 33). All the loops measured from Traders Member samples saturate below 0.8 T. When plotted on the Day plot, the M_{rs}/M_s and H_{cr}/H_c ratios for the Traders Member samples range from nearly single-domain (SD) to multi-domain (MD) behavior (Figure 35). The large scatter of the data points on the Day plot suggests complex magnetic fabric compositions for the Traders Member samples.

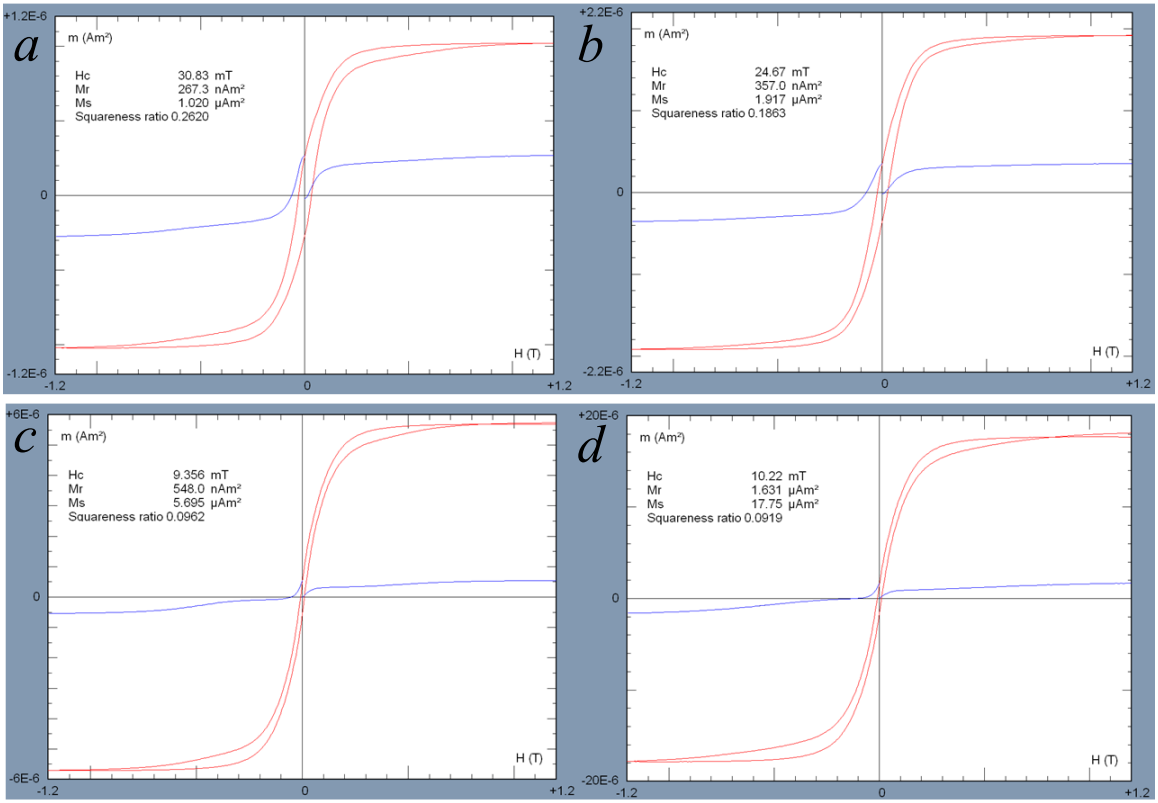

Figure 33: Magnetic hysteresis data from the Traders Member samples: a) FR01A, b) FR01B, c) FR02B, and d) FR02C. Red lines show induced magnetic moment (m) versus applied field (H). Blue lines show the acquisition of isothermal remanent magnetization (for positive H) and backfield demagnetization of the saturation remanent magnetization for negative H). Abbreviations: H_c, coercivity; M_s, saturation magnetization; M_{rs}, saturation remanent magnetization.

The Curry Member samples also produced a wide variety of hysteresis loops with the majority of irregular loops of both potbellied and wasp-waisted varieties (Figure 34). However, in general, the loops are wider than those measured from the Traders Member samples and some of them do not saturate in the maximum applied magnetic field (e.g., Figure 34e). The inflections on the DC demagnetization and IRM curves are more strongly expressed for many specimens of Sites CH0 and LH (Figure 34). Together, these observations indicate that the relative amount of hematite in the Curry Member is higher than in the Traders member.

The M_{rs}/M_s and H_{cr}/H_c ratios from Site CF0 suggests single-domain (SD) to pseudo-single-domain (PSD) magnetic carriers. This likely reflects the larger threshold for SD behavior for hematite. At the same time, the hysteresis ratios for Site CF1 are tightly clustered and plot towards the MD field on the Day plot (Figure 35). The more MD behavior of these samples is consistent with the thermomagnetic data (less pronounced Hopkinson peaks).

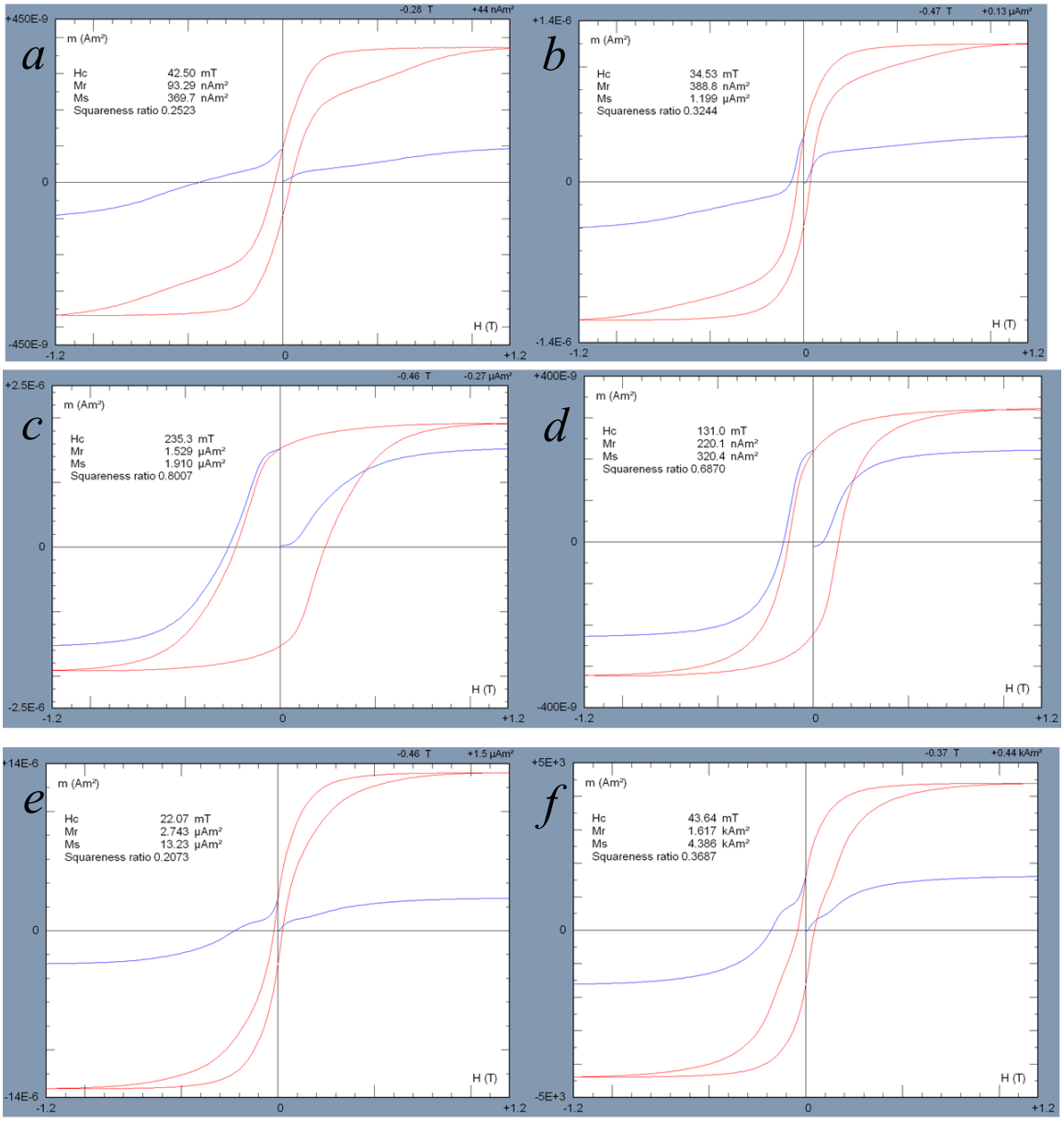

Figure 34: Magnetic hysteresis data from the Curry Member samples: a) LH01, b) LH02, c) CF01, d) CF03, e) CF04, and f) CF05. Blue lines show the acquisition of isothermal remanent magnetization (for positive H) and backfield demagnetization of the saturation remanent magnetization (for negative H). Abbreviations: H_c, coercivity; M_s, saturation magnetization; M_{rs}, saturation remanent magnetization.

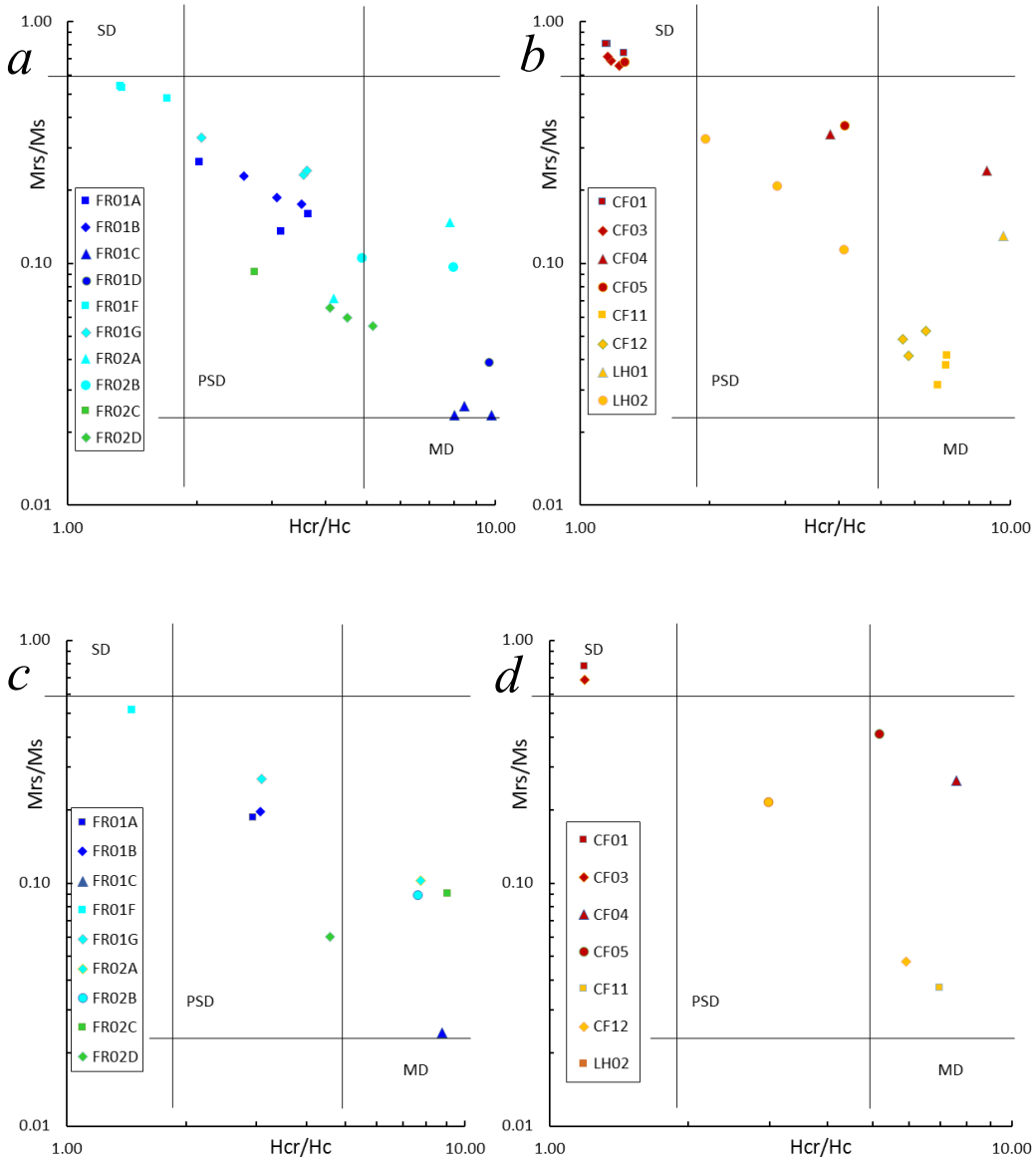

Figure 35: Magnetic hysteresis properties (Day plot) measured from individual specimens from the a) Traders Member and b) Curry member samples. The sample means for the c) Traders Member and d) Curry member samples. FR01D, FR01E, and LH01 plot off their respective Day Plots. Abbreviations are the following: SD, single domain; PSD, pseudo-single domain; MD, multidomain; Mrs, saturation remanence; Ms, saturation magnetization; Hc, coercivity field; and Hcr, coercivity of remanence.

4.5 First-Order Reversal Curve (FORC) Analyses

First order reversal curves (FORCs) were measured from several samples selected to represent the different types of observed magnetic hysteresis loops. For the Traders Member, FORC diagrams were obtained for sample FR01B (a potbellied loop), FR01C (a regular narrow loop), FR01D (a narrow potbellied loop), FR01F (a wide regular loop), and FR01G (a relatively wide potbellied "goose-neck" loop) (Figure 36).

The FORC distribution for sample FR01B is elongate, well separated from the vertical (H_u) axis, and tilted about 30° with respect to the horizontal (H_c) axis (Figure 36a,b). Correspondingly, the distribution maximum is located below the H_c axis at $H_c \approx 30$ mT and $H_u \approx -5$ mT. The distribution suggest the presence of two strongly interacting phases with different coercivity distributions. For this sample, the phases likely are PSD magnetite with a relatively small grain size and hematite.

Samples FR01C and FR01D manifest similar "three-lobe" FORC diagrams with the maximum located close to the origin and are characterized by a significant spread along the H_u axis (Figure 36c,d and Figure 37a,b, respectively). The "horizontal lobe" on both diagrams extending towards higher H_c values exhibits a small tilt respect to the H_c axis. Such three-lobe FORC diagrams are typical for large PSD or multidomain magnetite. However, the small tilt of the third lobe may indicate the presence of and interaction with some amount of hematite. The hematite signal is probably more significant in sample FR01D as indicated by the location of the distribution maximum slightly further away from the diagram origin in comparison with sample FR01C. Interestingly, the thermomagnetic curves also show a stronger hematite signal for sample FR01D (Figure 28d).

The FORC distribution for sample FR01F has a single maximum at $H_c \approx 60$ mT and $H_u \approx -15$ mT (Figure 37c,d). The FORC distribution is close to one typical for interacting nearly SD grains (e.g., Roberts et at., 2000) but is somewhat asymmetrical resembling a lower case sigma (σ) and shifted down from the H_c axis. The asymmetry is likely to reflect interaction between magnetite and hematite within the sample similar to FR01B. For FR01F, however, the FORC diagram is dominated by the presence of nearly

SD grains as indicated by a narrow ridge along the H_c axis extending above 200 mT (Figure 36d).

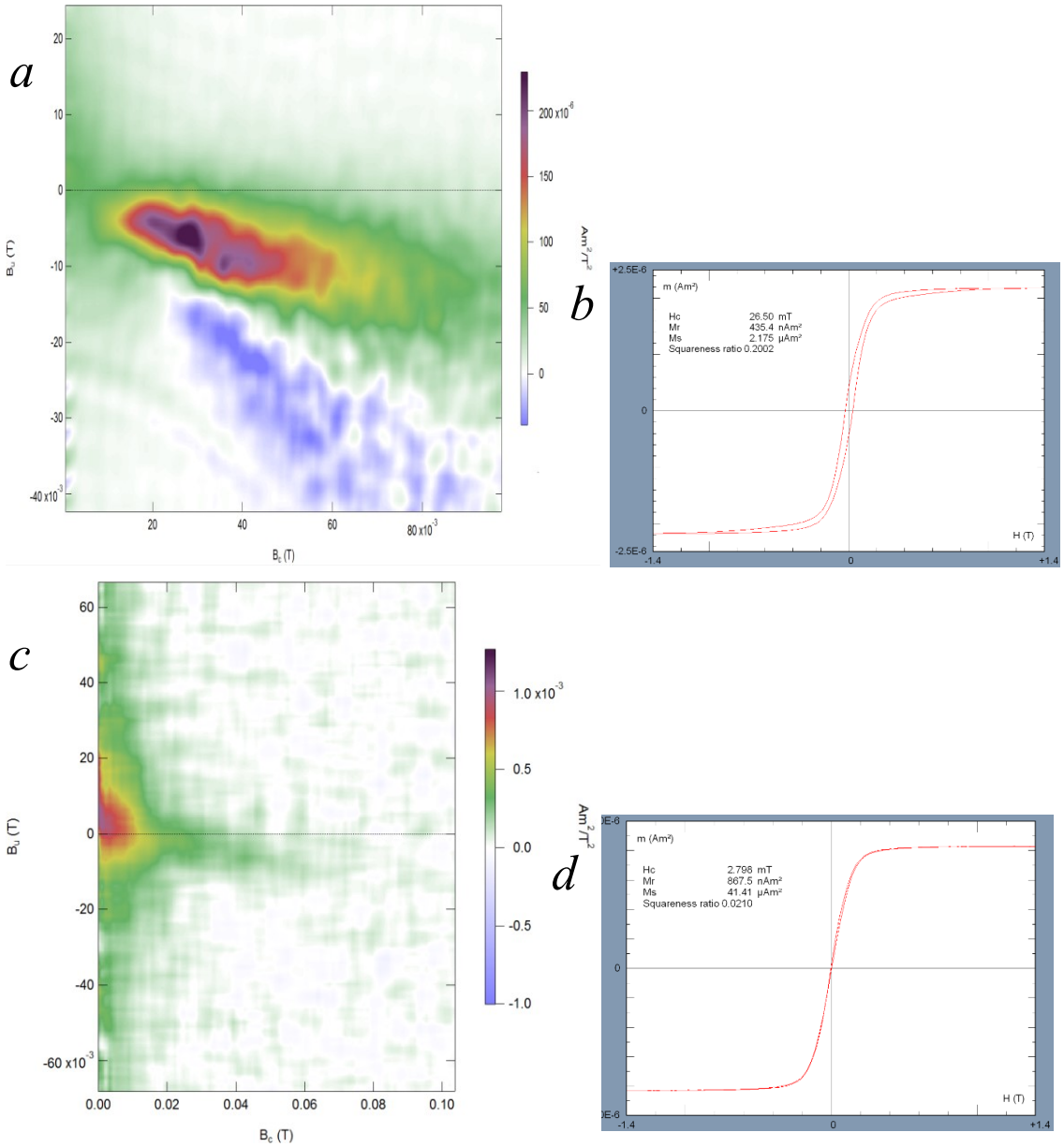

Figure 36: First-order reversal curve (FORC) distributions measured from the Trader Member samples a,b) FR01B, c,d) FR01C, with corresponding bulk hysteresis loops. Smoothing factor SF = 6.

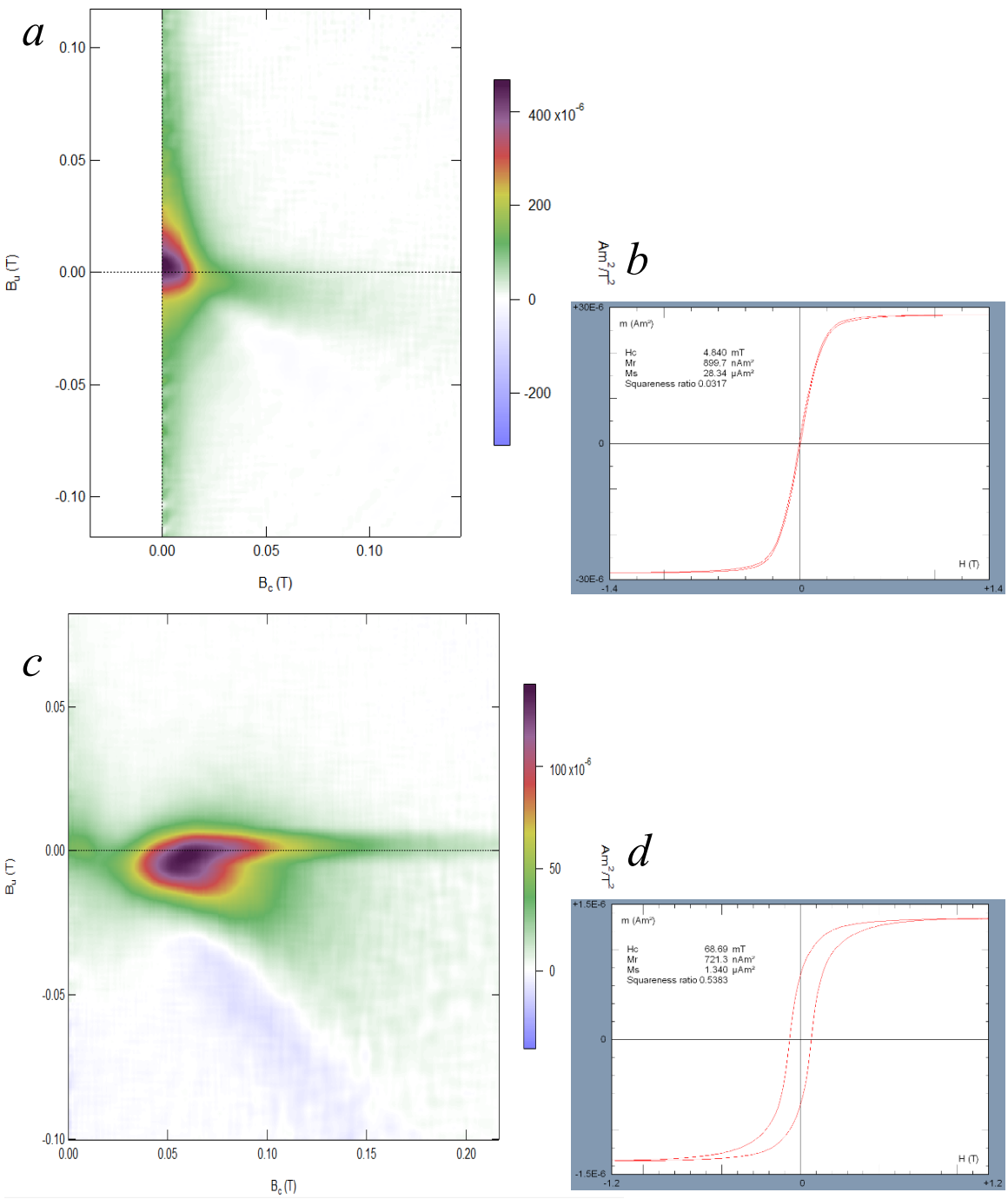

Figure 37: First-order reversal curve (FORC) distributions measured from the Trader Member samples a,b) FR01D, c,d) FR01F, with corresponding bulk hysteresis loops. Smoothing factor SF = 6.

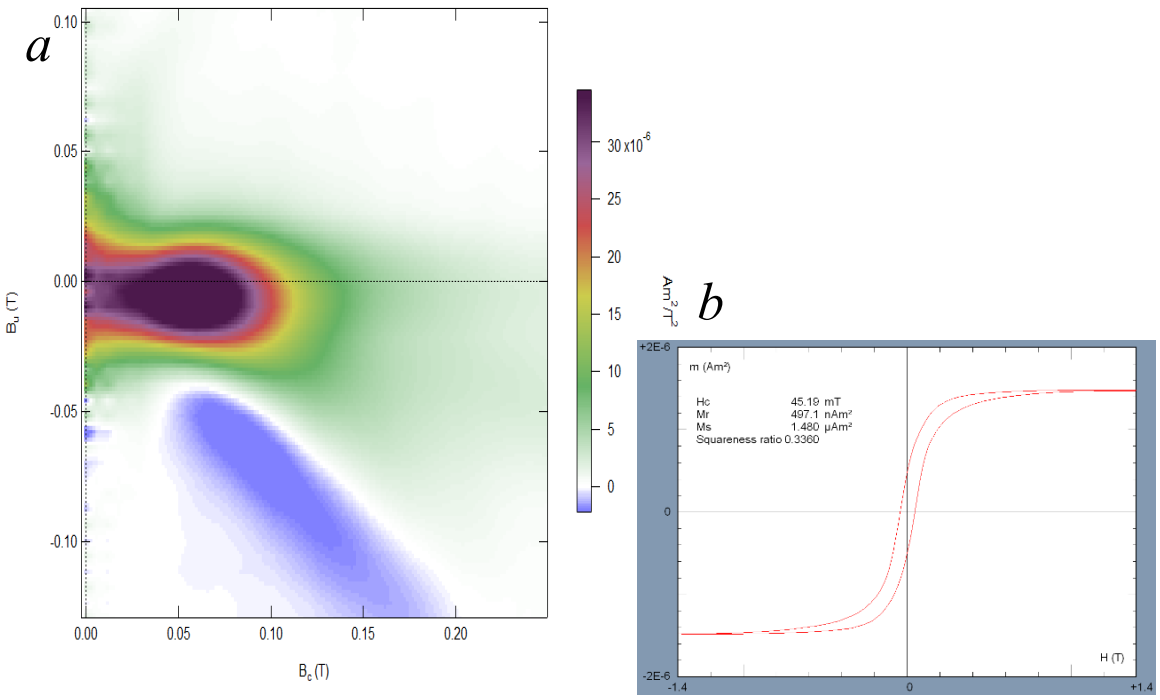

Figure 38: a) First-order reversal curve (FORC) distributions measured from the Trader Member sample FR01G, with corresponding b) bulk hysteresis loops. Smoothing factor SF = 6.

The FORC distribution for sample FR01G has a single broad maximum at $H_c \approx 60$ mT and $H_u \approx -10$ mT (Figure 38), slightly shifted down and asymmetrical with respect to the H_c axis. Together with a not saturated hysteresis loop, this distribution likely reflects a relatively larger amount of hematite in the sample.

For the Curry Member samples, FORC datasets were measured from CF01, CF03 (wide, non-saturated wasp-waisted loops), CF05 (a "classic" wasp-waisted loop), CF11 (a narrow slightly wasp-wasted loop), and LH02 (a relatively wide potbellied "goose-neck" loop but narrower than for FR01F) (Figure 41c).

The FORC distribution for sample CF01 has a narrow elongate shape tilted down from the Hc axis and entirely located in the lower (negative H_u) part of the diagram. The maximum is not well expressed and located at $H_c \approx 60$ mT and $H_u \approx -25$ mT (Figure 38). The FORC distribution for sample CF03 is generally similar to that for CF01 also located below the H_c axis but has a more expressed maximum (at $H_c \approx 100$ mT and $H_u \approx -20$ mT) and is less tilted with respect to the H_c axis (Figure 40a,b). The distributions suggest the

presence of interacting SD particles of primarily uniform mineral composition. The lack of saturation in 1.4 T suggests hematite as the primary magnetic carrier. This is consistent with the thermomagnetic data which do not show the Verwey transition during the initial low-temperature κ(T) run.

Sample CF05 exhibits two maximum peaks in its FORC distribution, one at the origin (suggesting a soft, PSD magnetic phase) and a weaker peak at $H_c \approx 160$ mT and $H_u \approx -20$ mT (Figure 40c,d). The two peaks correspond to two different ferromagnetic phases with very different coercivities. Thermomagnetic analyses indicated that the minerals are PSD magnetite and hematite. The clear separation between the peaks is usually interpreted as an indicator of a weak interaction between the two phases.

The FORC distribution for sample CF11 has a single maximum peak at the origin and stretches along the H_u axis, indicating the presence of large PSD or MD grains (Figure 41a,b).

The FORC distribution for LH02 has a single maximum at $H_c \approx 30$ mT and $H_u \approx -5$ mT and shape slightly resembling the sigma-shape observed for sample FR01F (Figure 41c,d). The distribution is, however, more symmetrical suggesting a weaker interaction between magnetite and hematite.

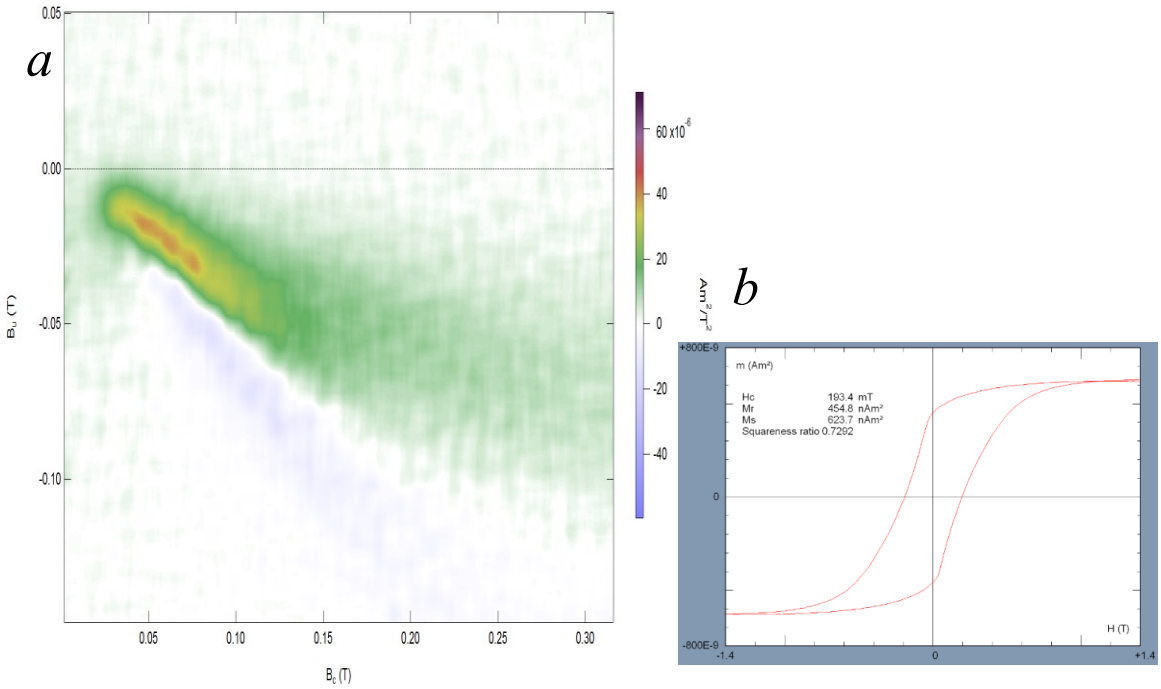

Figure 39: a) First-order reversal curve (FORC) distributions measured from the Curry Member sample CF01, with corresponding b) bulk hysteresis loops. Smoothing factor SF = 6.

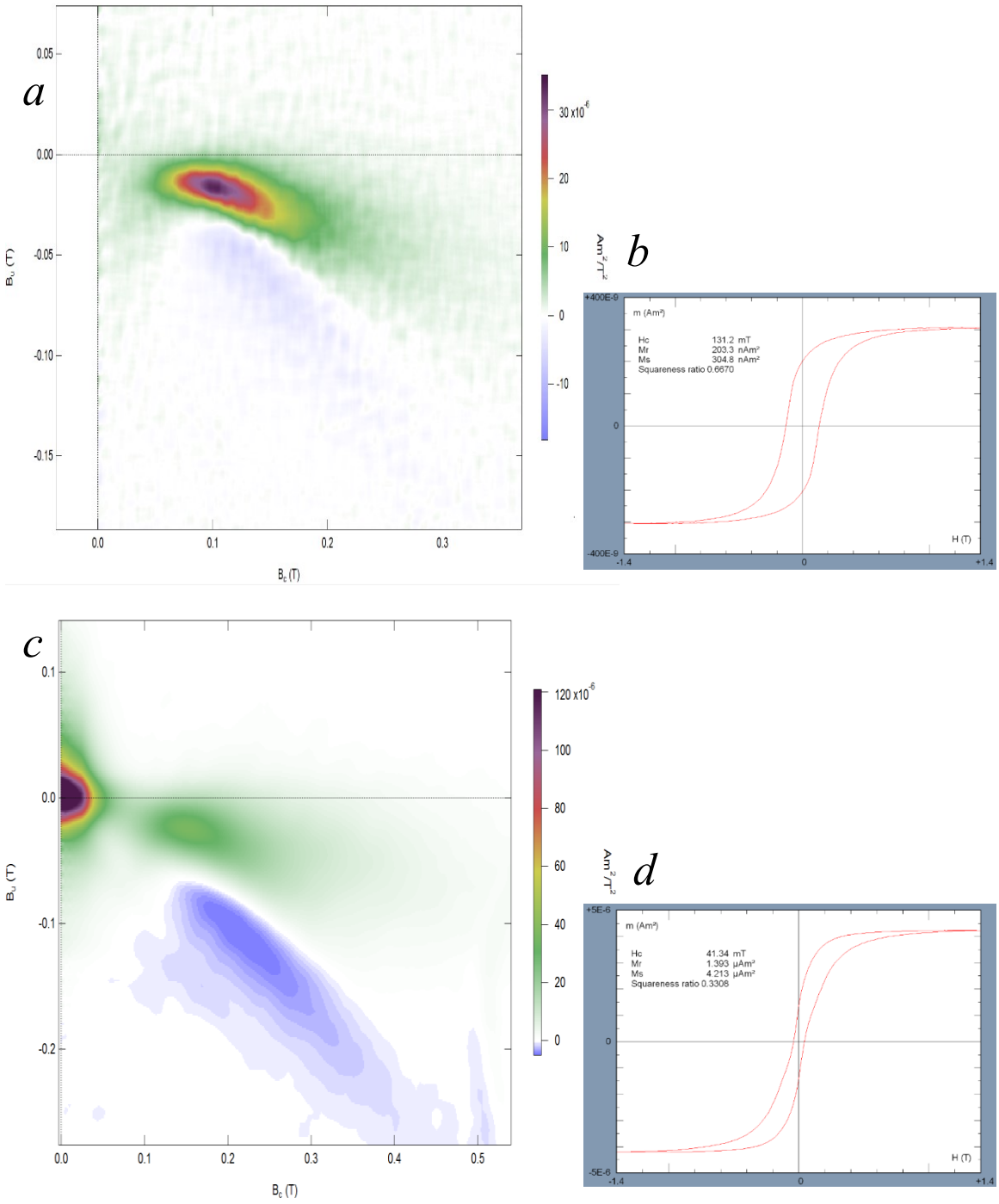

Figure 40: First-order reversal curve (FORC) distributions measured from the Curry Member samples a,b) CF03, c,d) CF05, with corresponding bulk hysteresis loops. Smoothing factor SF = 6

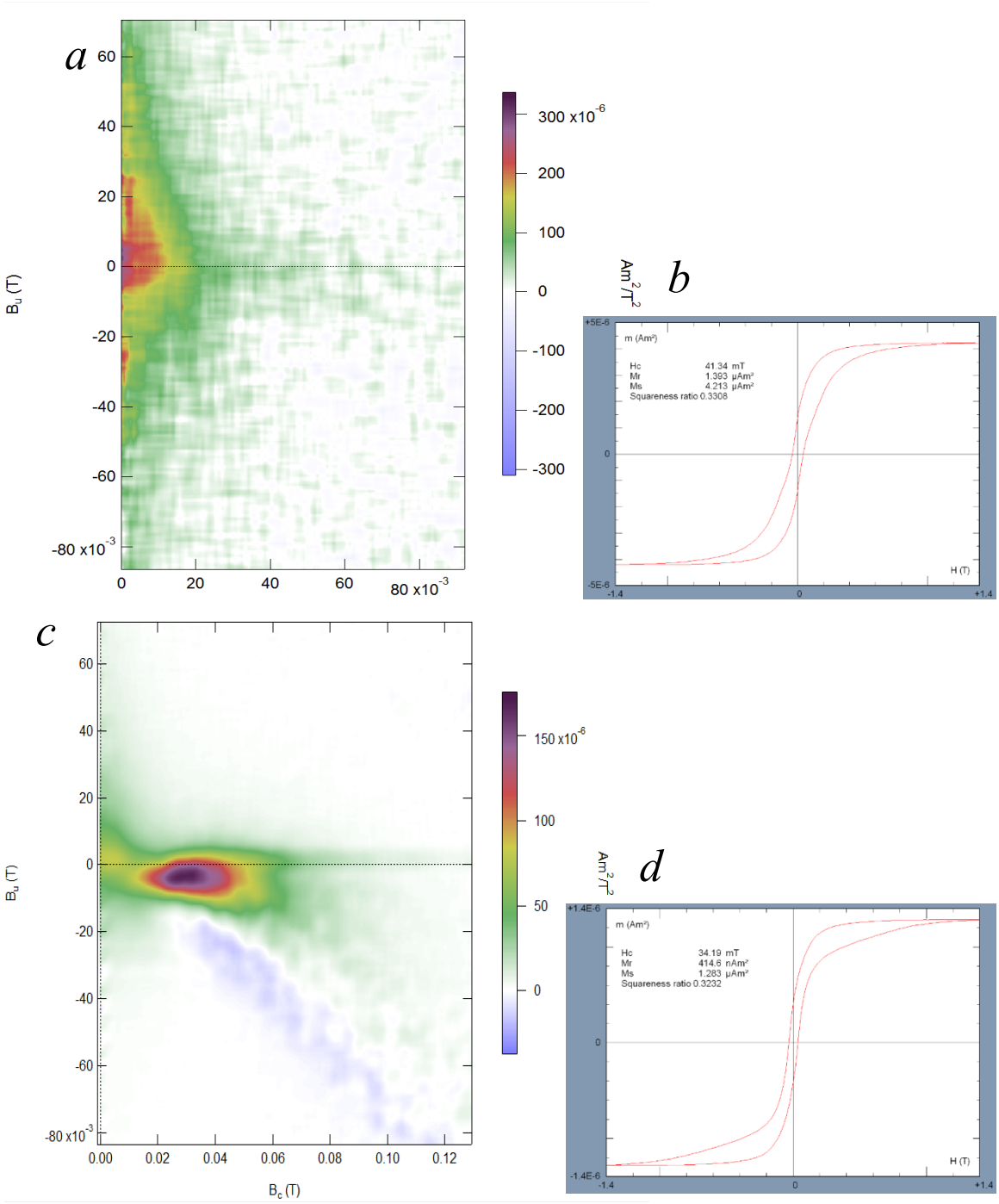

Figure 41: First-order reversal curve (FORC) distributions measured from the Curry Member samples a,b) CF11, and c,d) LH02 with corresponding bulk hysteresis loops. Smoothing factor SF = 6.

4.6 Anisotropy of Magnetic Susceptibility Analyses (AMS)

The AMS and bulk susceptibility analyses were conducted on 10 samples of the Traders Member and 14 samples of the Curry Member (Table 2). The volume normalized mean bulk susceptibility is 31.77 ± 15.64 (1 σ) · 10^{-3} SI for the Traders Member (without anomalies FR01C and FR01E) with a median of 31.23 · 10^{-3} SI, and 19.93 ± 20.46 (1 σ) · 10^{-3} SI for the Curry Member with a median of 14.44 · 10^{-3} SI. The high bulk susceptibilities are consistent with the presence of ferromagnetic mineral such as magnetite or hematite.

Table 2: Summary of AMS results for the Traders and Curry Members. K_m = mean magnetic susceptibility; L = magnetic lineation; F = magnetic foliation; Pj = corrected degree of anisotropy; T = shape parameter; Declination (dec) and inclination (inc) of means of the maximum (K1), intermediate (K2), and minimum (K3) susceptibility axes in degrees.

Name	Km*10-3 (SI)	L	F	Pj	T	K1dec (°)	K1inc (°)	K2dec (°)	K2inc (°)	K3dec (°)	K3inc (°)
FR01B	9.45	1.051	1.207	1.285	0.581	20	2.6	288.7	27.2	115.1	62.7
FR01C	299.97	1.027	1.208	1.265	0.753	224.7	7.9	320.3	35.3	123.8	53.6
FR01E	0.29	1.006	1.159	1.190	0.922	156.1	8.4	251.3	31.5	53	57.1
FR01F	17.65	1.064	1.218	1.311	0.522	208.4	16.4	104.1	39.9	315.8	45.5
FR02B1	54.19	1.022	1.264	1.328	0.831	155	3.7	245.9	14.1	50.6	75.4
FR02B2	51.49	1.013	1.258	1.314	0.892	163.4	0.2	253.5	8.7	72.4	81.3
FR02C1		1.043	1.228	1.304	0.657	88.6	2.9	358.3	5.3	207.5	84
FR02C2	23.44	1.049	1.242	1.325	0.638	89.7	1.1	359.7	0.2	257.9	88.9
FR02C3	18.63	1.061	1.245	1.341	0.572	85.1	2	175.3	6.1	336.8	83.5
FR02D1	40.29	1.048	1.284	1.376	0.683	251.3	2.2	160.8	14.1	349.9	75.8
FR02D2	39.02	1.039	1.280	1.362	0.730	63.2	1.9	333.1	2.7	188.9	86.7
Averages	55.44	1.038	1.237	1.310	0.712	141.7	4.6	249.3	18.0	186.4	71.1
Average w/o C and E	31.77	1.04	1.25	1.33	0.68	129.51	3.76	240.14	14.13	210.93	74.98
Median w/o C and E	31.23	1.05	1.25	1.33	0.66	122.35	2.10	249.70	11.40	223.40	78.55
Std Dev w/o C and E	15.64	0.02	0.03	0.03	0.12	73.14	4.87	82.55	12.52	113.43	13.53
CF01A	1.48	1.029	1.003	1.035	-0.815	352.9	3.8	96.9	74.6	261.9	14.9
CF03A	0.10	1.012	1.001	1.014	-0.828	191.9	21.1	33.5	67.5	284.8	7.5
CF03B	0.42	1.010	1.005	1.016	-0.302	200.3	10.9	54.7	76.9	291.7	7.2
CF04A	14.71	1.007	1.111	1.134	0.874	232	23.9	135	15.3	15.4	61.1
CF04B	21.39	1.001	1.111	1.130	0.979	222.4	26.5	126.3	12.1	14	60.5
CF05A	3.11	1.024	1.066	1.094	0.464	359.8	12.4	251.4	55	97.7	32.1
CF11A	23.72	1.066	1.094	1.167	0.165	162.9	43	67.9	5.4	332.2	46.5
CF11B	33.67	1.044	1.098	1.150	0.371	355.6	61	121.6	18.1	219.1	21.8
CF12A	59.79	1.029	1.145	1.192	0.646	197.7	20	103	12.8	342.3	66
CF12B	68.37	1.038	1.141	1.194	0.561	201	18.1	105.4	16.7	335.4	65
LH01A	5.95	1.106	1.113	1.231	0.032	271.2	38	56.8	46.6	166.6	17.8
LH01B	20.27	1.095	1.130	1.238	0.147	269.4	39.9	58.6	45.7	165.6	16
LH02A	14.17	1.148	1.297	1.498	0.305	1.9	39.8	165.4	49	265	8.3
LH02B	11.91	1.140	1.259	1.442	0.274	15.2	41.3	193.9	48.7	284.7	0.6
Averages	19.93	1.054	1.112	1.181	0.205	216.7	28.6	112.2	38.9	219.7	30.4
Median	14.44	1.034	1.111	1.159	0.290	211.7	25.2	104.2	46.2	263.5	19.8
Std Dev	20.46	0.048	0.083	0.137	0.526	105.4	15.2	58.2	24.1	108.0	23.4

For all measured samples, the shape parameter (T) was plotted as a function of the corrected degree of magnetic anisotropy (Pj) (the Jelinek plot; Jelinek, 1981). The Jelinek plots for the Traders Member (Figure 42a) plot an oblate shape anisotropy parameter for the specimens with a cluster of somewhat high degree of anisotropy. This implies the Traders Member specimens have an oblate shape of the susceptibility ellipsoid, which is to be expected for BIF. The shape parameter is also consistently between 0.5 and 1.

Plotting the normalized mean bulk susceptibility (K_m) against the degree of magnetic anisotropy (Pj) allows investigation as to whether anisotropy is a result of the ferromagnetic mineral volume percentage in the rock or the result of strain applied during the rocks lifetime (for example from the nearby South Range fault). The Traders Member specimens plot (Figure 42b) shows no correlation between Pj values and amount of ferromagnetic minerals ($R^2 = 0.1231$).

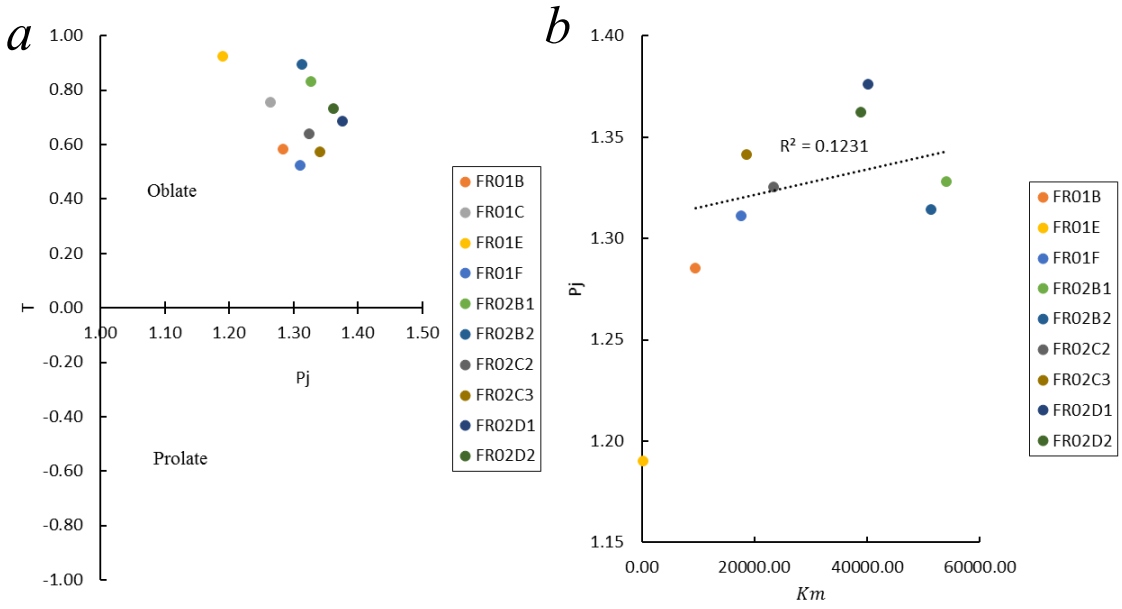

Figure 42: Anisotropy of magnetic susceptibility (AMS) data for the Traders Member samples. a) Jelinek Plot (Pj vs T); b) Mean bulk susceptibility (Km) versus the degree of anisotropy (Pj). FR01C is not shown due to its very high bulk susceptibility (~300,000 SI).

The Curry Member are mainly oblate, but three specimens (CF01A, CF03A, CF03B) are prolate (Figure 43a), which is not typical for a BIF. It is noteworthy that the prolate shape parameter specimens also exhibit smaller degree of anisotropy (Pj). These specimens also lacked a Verwey Transition on their thermomagnetic curves, suggesting that magnetite may not be present in large amounts to direct the anisotropy.

As with the Traders plot, the Km vs Pj plot based on the Curry Member data (Figure 43b) does not show a good correlation between ferromagnetic mineral volume amount and degree of magnetic anisotropy. It is worth noting that the correlation is less than that of the Traders Member (R^2=0.0303).

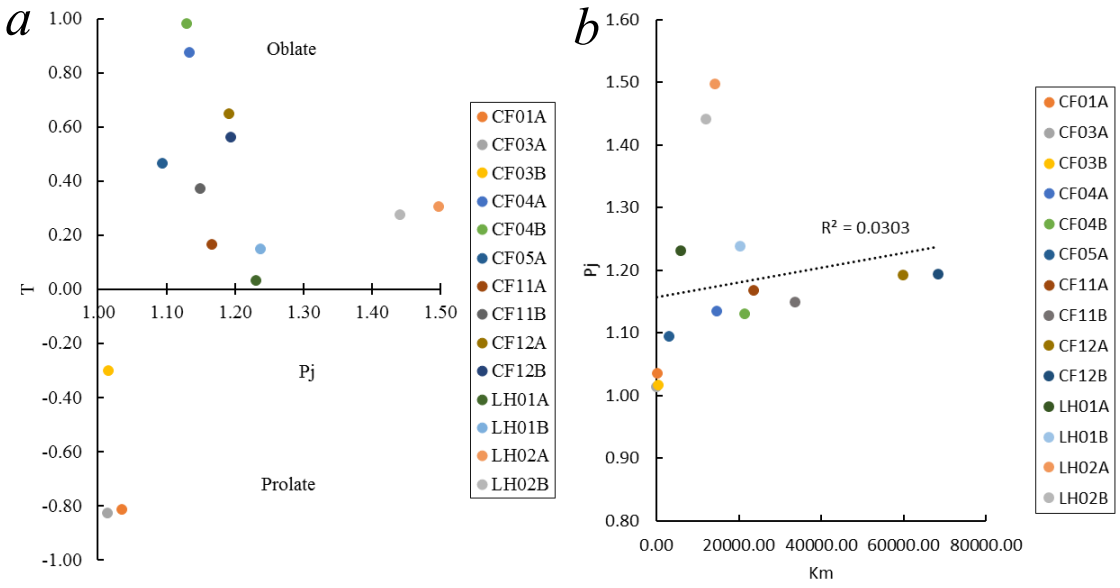

Figure 43: Anisotropy of magnetic susceptibility (AMS) data for the Curry member samples. a) Jelinek Plot (Pj vs T) b) Mean bulk susceptibility (Km) vs degree of anisotropy (Pj).

The Traders and Curry Members AMS data were plotted on equal area plots (Figures 44ab and 44cd, respectively) to compare the bedding plane to anisotropy. Since sites LH and CF0/CF1 have different bedding planes, only specimens from sites CF0 and CF1 were plotted against the bedding plane as not enough samples from site LH were taken. This comparison indicates a good correlation between bedding and anisotropy,

which is expected for BIF. Inverse fabrics also exists at each site (K1 squares plotted near K3 circles) which could indicate SD grains.

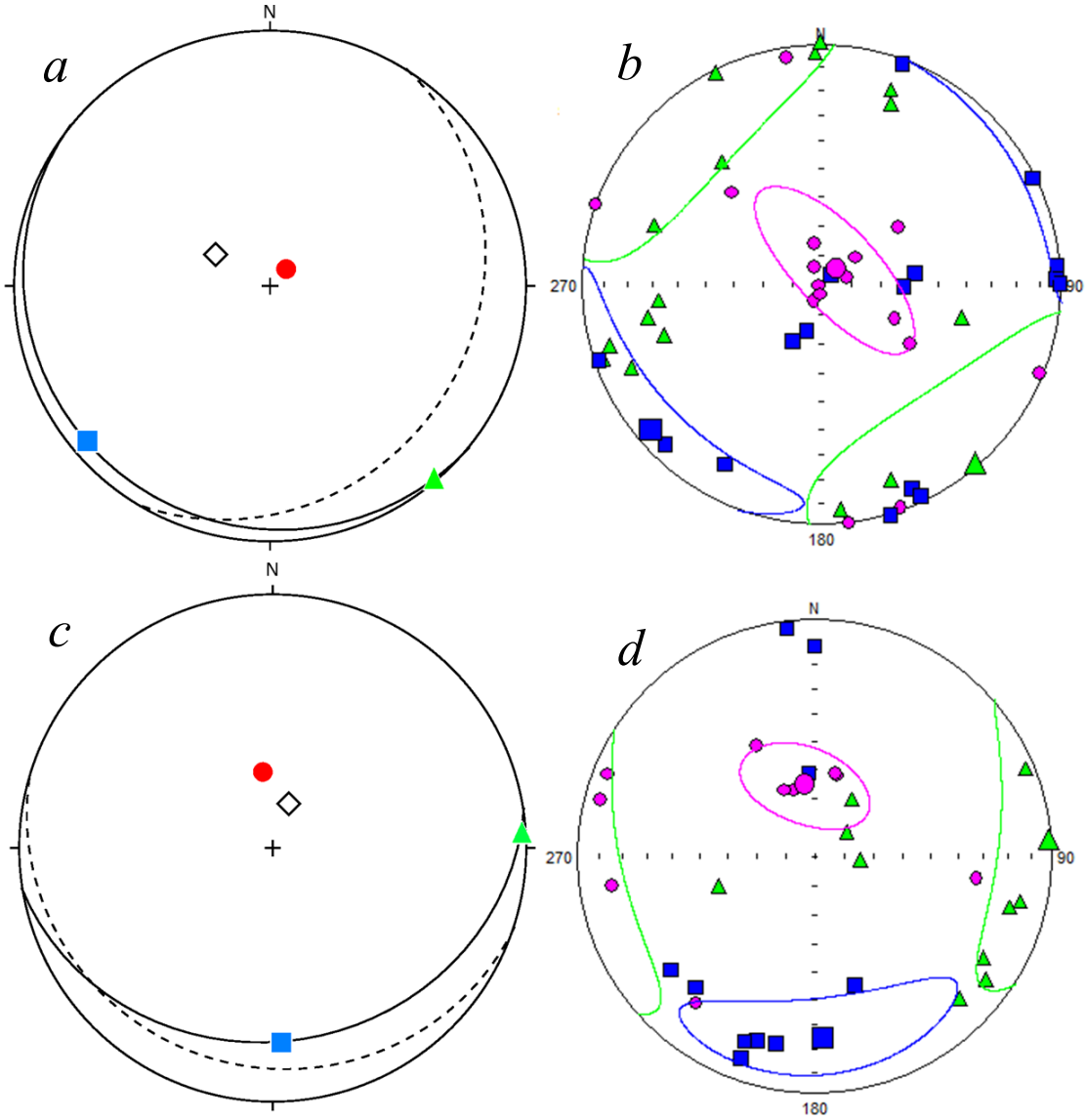

Figure 44: Lower hemisphere equal-area projections of mean AMS directional data. a) Traders projection with bedding, b) Traders projection with error ellipsoids c) Curry projection with bedding, and d) Curry projection with error ellipsoids. K1, K2, and K3 are defined by blue squares, green triangles, and red circles respectively. The common great

circle (solid line) passing through K1 and K2 defines the magnetic foliation (F). Orientation of average bedding plane plotted as pole (black diamond) and a great circle (dashed line).

4.7 Scanning Electron Microscopy (SEM)

Backscatter electron (BSE) and secondary electron (SE) images as well as energy dispersive X-ray spectroscopy (EDS) spectra analysis were obtained for one sample of the Curry (CF01) and Traders (FR01A) Members. BSE and SE images were taken to investigate the shape, abundance, and lamination of magnetic grains in the sample. EDS spectra analyses were performed to investigate the element composition of magnetic grains.

The Traders Member sample showed characteristic BIF iron-rich lamination at finer detail (Figure 45). There are two different iron oxide grains within the sample that vary both in qualitative EDS data as well as in grain structure. The more common iron oxide grains have an elongated, cubic structure that closely resembles magnetite (Figure 46a). The other, less common, type of iron oxide grain does not appear to have the sharp cubic structure common in the magnetite grains (Figure 46a). A qualitative EDS spectra analysis shows elevated levels of elemental iron as opposed to elemental oxygen. Without a quantitative analysis of the grains, a precise definition of the mineral could not be ascertained. However, a higher Fe content is consistent with hematite.

The matrix component of the Traders Member BIF is represented by a complex combination of cherts and clays. The primary matrix is basic chert, but there exists small blotches of other minerals such as a calcium iron silicate-phosphate (spectrum 17, Figure 46b), potentially Harrisonite, $CaFe^{2+}_6(SiO_4)_2(PO_4)_2$; (Roberts et al., 1993). A sugary textured, aluminum and potassium rich mineral with varying degrees of iron content (spectrum 21, Figure 47a,b) may be orthoclase (a potassium aluminum silicate, e.g., $KAlSi_3O_8$). A spotted magnesium, aluminum silicate oxide mineral was also present (spectrum 30, Figure 47c,d) which may be a Mg-diffused quartzite. The presence of Fe-rich clays was also observed.

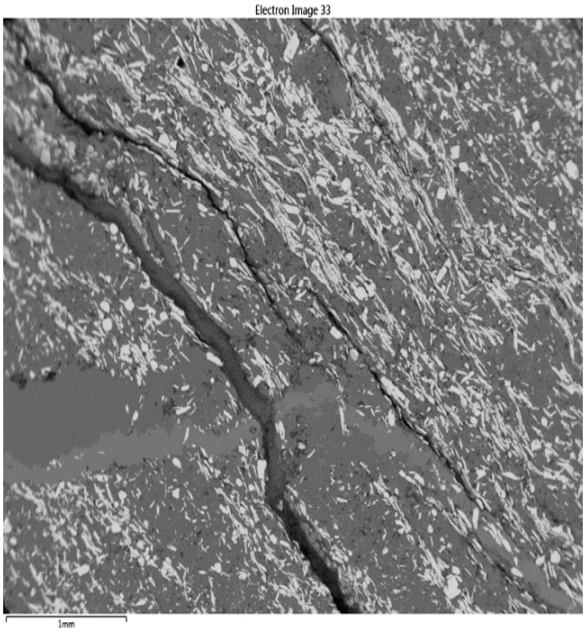

Figure 45: Backscatter electron image of the Traders Member sample FR01A showing alternating layers of iron oxide (lighter areas) and chert (darker areas).

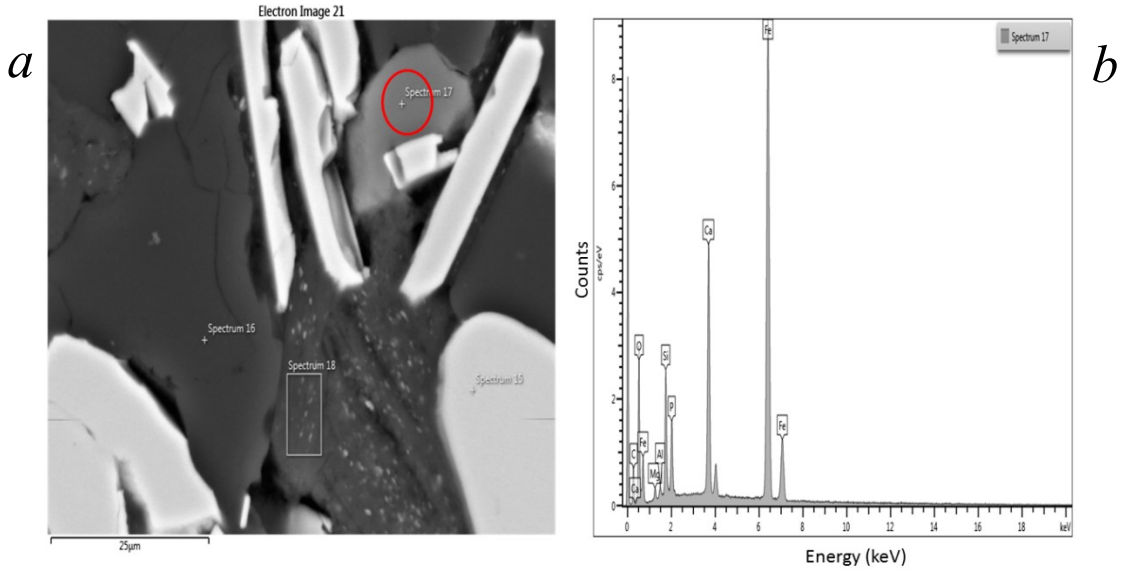

Figure 46: a) Backscatter electron images and corresponding b) electron dispersive spectra (EDS) of the Traders Member sample FR01A. Comparison of two iron oxide grains, one cubic in the top center and one not in the bottom right. A blotch in top left is possibly Harrisonite. The areas from which the EDS spectra were taken are shown by red circles.

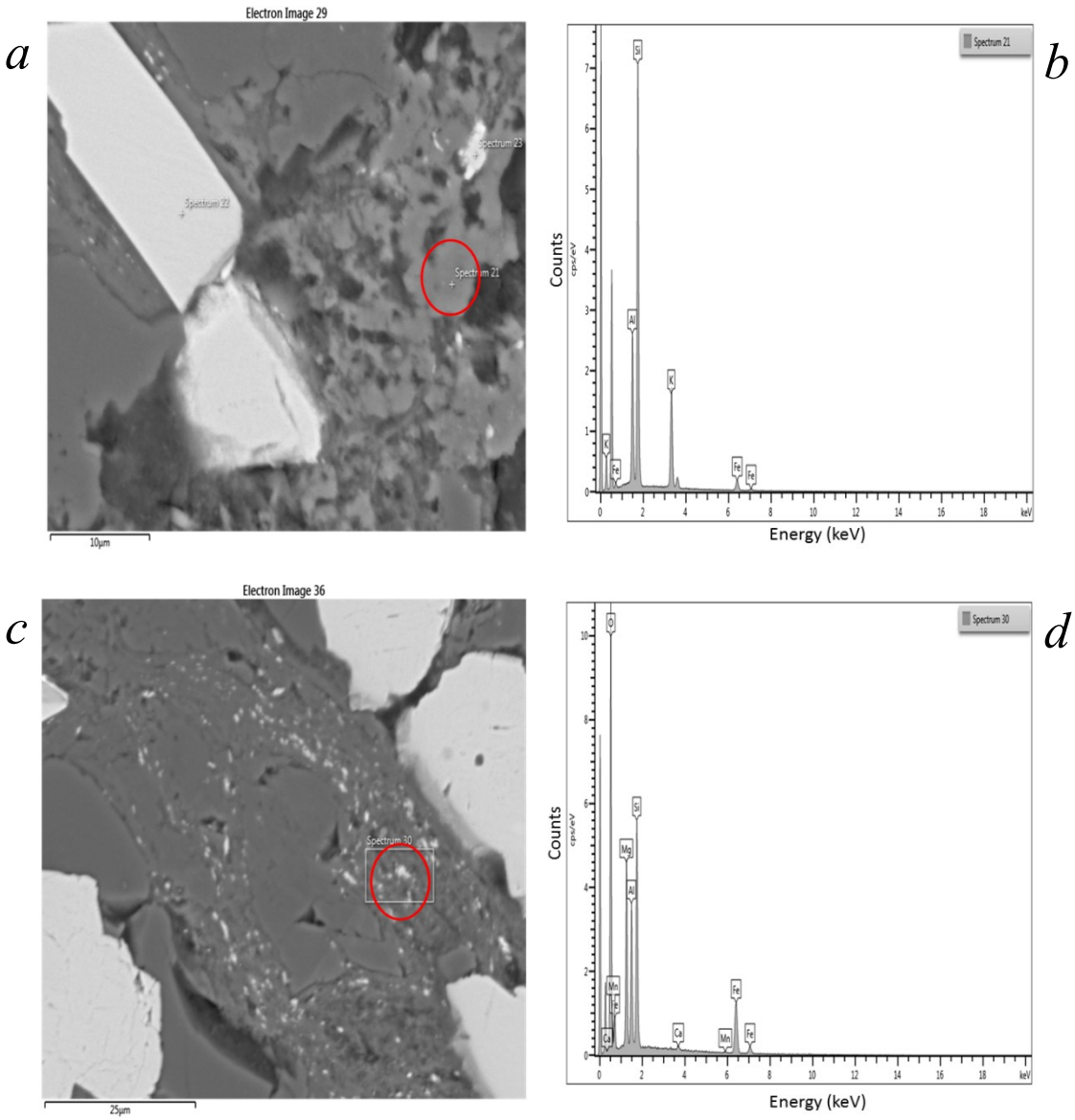

Figure 47: Backscatter electron images and corresponding electron dispersive spectra (EDS) of the Traders Member sample FR01A. a,b) Orthoclase, c,d) Mg-diffused quartzite. The areas from which the EDS spectra were taken are shown by red circles.

The Curry Member does not have characteristic BIF iron-bearing grain lamination. Instead, most iron oxide is massive in appearance (Figure 48a,b). There are also noticeable grains of iron oxide that are not massive and have a different EDS spectra (Figure 48c,d).

These grains are less abundant then the massive iron oxide, and have higher levels of iron than oxygen in a quantitative analysis compared to the massive iron areas.

The matrix component of the Curry Member BIF is primarily comprised of a basic chert. A minority of the non-iron oxide minerals include platey structured silicate oxide with magnesium and aluminum elements (Spectrum 4) (Figure 49a,b). Among the platey mineral exist an iron oxide mineral with a sugary appearance that has hints of magnesium and aluminum (Spectrum 12) (Figure 49c,d). There are small flecks, usually around 2.5 μm across, of an iron tin oxide (Spectrum 8) (Figure 50a,b).

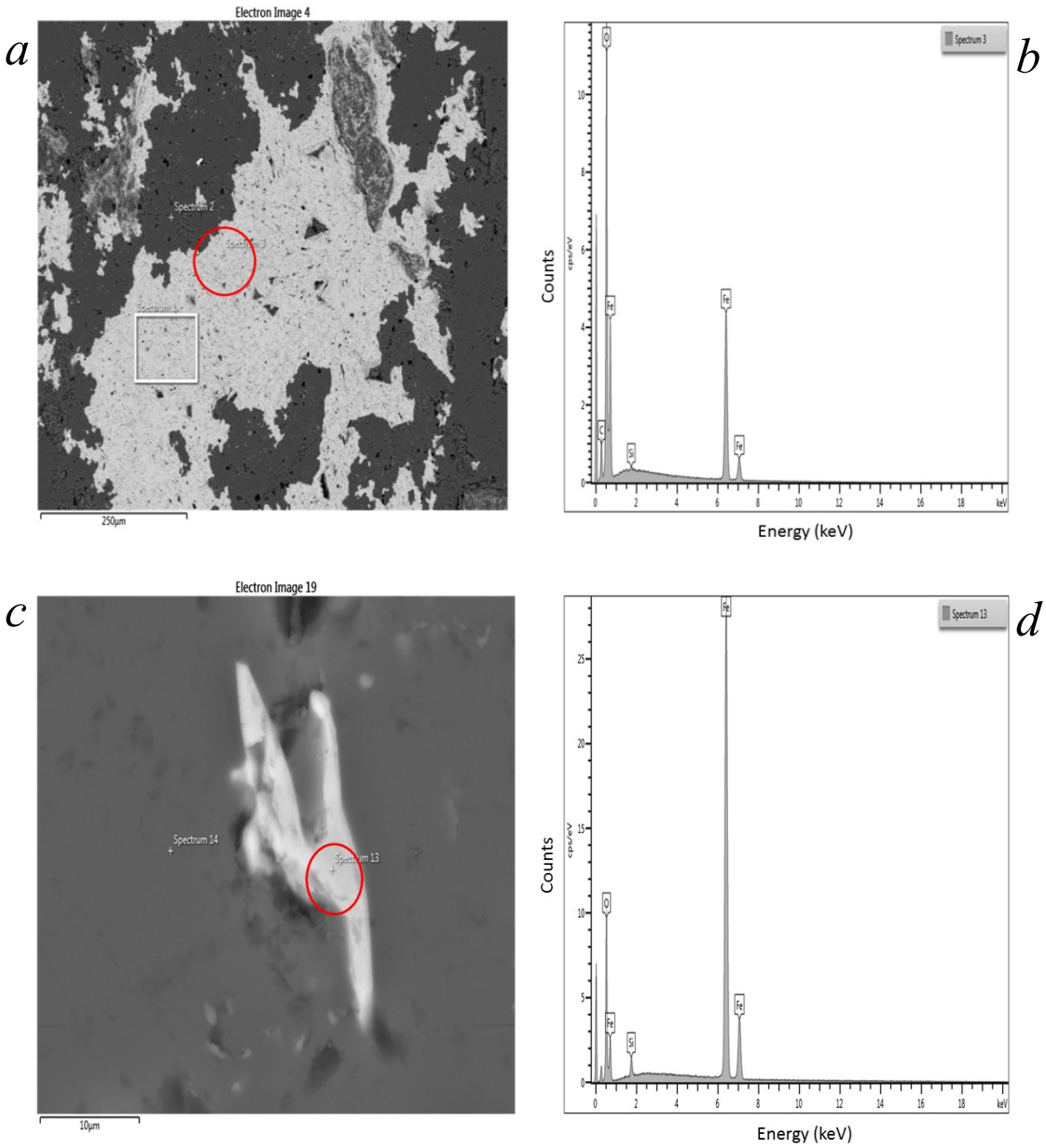

Figure 48: Backscatter electron images and corresponding electron dispersive spectra (EDS) of the Curry Member sample CF01. a,b) A massive iron oxide cluster, probably, magnetite, c,d) A separate iron oxide grain, probably, hematite. The areas from which the EDS spectra were taken are shown by red circles.

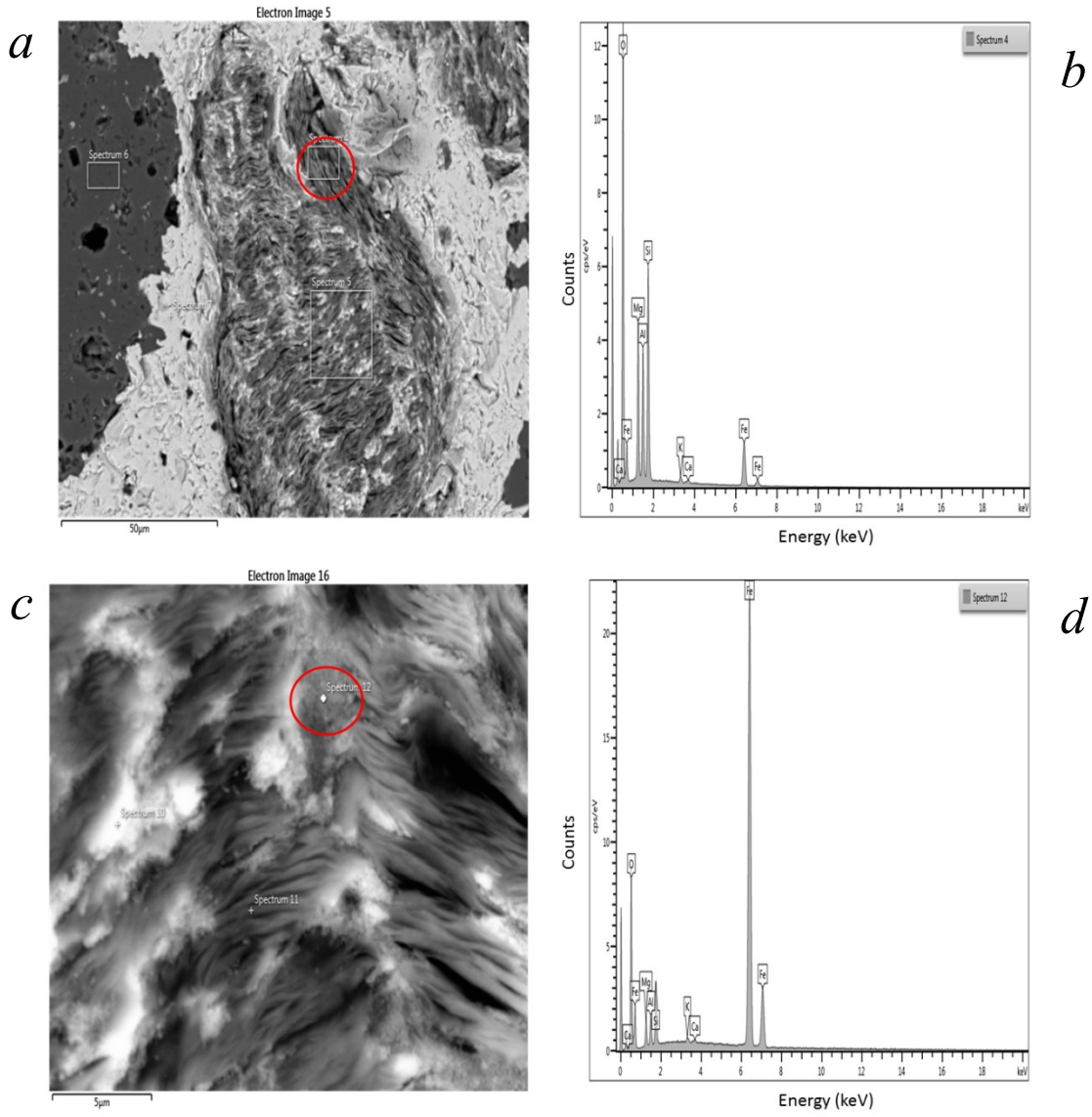

Figure 49: Backscatter electron images and corresponding electron dispersive spectra (EDS) of the Curry Member sample CF01. a,b) Platey mineral, probably, hematite. c,d) Zoom in on an area of sugary texture material within the platey mineral. The areas from which the EDS spectra were taken are shown by red circles.

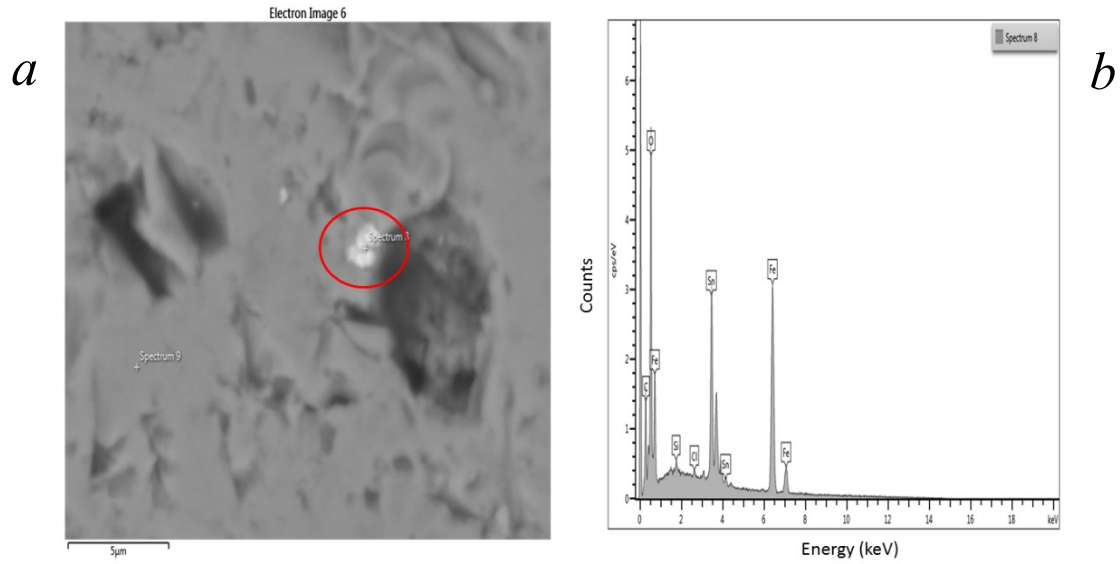

Figure 50: a) Backscatter electron images and corresponding b) electron dispersive spectra (EDS) of a small fleck of an iron-tin oxide from Traders Member sample CF01. The areas from which the EDS spectra were taken are shown by red circles.

5. Discussion

The results of our magnetic petrophysics investigation of the Vulcan Iron Formation reveal a distinct difference between its two constituent iron-bearing members, the Traders Member and the Curry Member. First, in contrast to the observation by Bayley et al (1966), we have observed a clear difference in the appearance of the two members. While the older Traders Member can be classified as a typical BIF, the younger Curry Member does not manifest an expressed and consistent banding and can be tentatively classified as a GIF. Additional microscopy analyses are required to confirm this classification. However, our observations are consistent with the observations made by Cumberlidge and Stone (1964) who investigated the Vulcan Formation exposures in the Groveland Mine, about 10 miles north of Iron Mountain. Although Cumberlidge and Stone (1964) did not use the now accepted classification of the Vulcan Formation members, they found two lithological iron-bearing sections one of which was uniformly banded iron formation with high percentages of magnetite (75-100%) and the other was only vaguely banded, magnetite poor (as low as 25%) iron formation. The correlation of these rocks with

the formations studied in this project (near Iron Mountain) is complicated due to the absence of access to the Groveland Mine site but analyses of geological relationships using geological maps suggests that the two sections identified by Cumberlidge and Stone (1964) may represent the Traders and Curry Members, respectively.

This interpretation is also supported by the results of our rock magnetic investigations. The well-banded Traders Member is characterized by a high relative amount of nearly-stoichiometric magnetite as evidenced by a large fraction of natural remanent magnetization lost upon low-temperature demagnetization (Figure 22) and by almost complete demagnetization of NRM by heating to 600 °C (Figure 23). In contrast, the Curry Member samples from Site CF0 show significantly lower loss of NRM upon LTD (Figure 22) and a substantial portion of NRM remains after temperature treatment to 600 °C (Figure 23). The obtained thermomagnetic, magnetic hysteresis, and FORC data also indicate much higher hematite-to-magnetite ratios in the magnetic Fe-oxide grains in the Curry Member versus the Traders Member. However, the two samples collected at Site CF1 (identified as the Curry member) show very different rock magnetic behavior. While the Sample CF11 characteristics are similar to those observed from the CF0 samples, the rock magnetic behavior of Sample CF12 closely resembles that of the Traders Member samples FR1 and FR2 (e.g., Figures 22 and 23). In particular, the data suggest that the hematite-to-magnetite ratios are dramatically different within one outcrop. Nevertheless, in general, our study shows that the members of the Vulcan Iron Formation can be differentiated by the hematite-to-magnetite ratios of the magnetic Fe-oxide grains.

The observed noticeable difference in magnetic petrophysical properties between the two iron-bearing members is striking because they are geographically and stratigraphically adjacent and have similar depositional ages. Assuming a low sedimentation rate (6 m/Ma; e.g., Barker et al., 2001), the accumulation of the 30-100 m Brier Member, which separates the Traders and Curry Members, could take ~5-15 Ma. However, the absence of lamination in the Brier Member suggests a faster sedimentation rate so the accumulation could take a significantly shorter time. If we assume that both members were formed via similar geologic mechanisms (e.g., Bekker et al., 2010), the petrophysical differences could be explained either by different depositional environments

or different metamorphic grades, or more likely both factors affecting the observed properties.

The Vulcan Iron Formation was deposited ~600 Ma after the Great Oxygenation Event when the iron-formation record is dominated by granular iron formations. However, some BIFs are also found for the same time period. One possibility is that the sequence of the Traders BIF member to the Brier shale/slate Member, to the Curry GIF Member reflects a geologically fast change from a deep ocean deposition (BIF), to a coastal deposition (shale), to a continental shelf (GIF) deposition. Taking into account that the deposition of the Vulcan Iron Formation occurred during the ongoing Penokean orogeny, such a fast ocean regression and transgression is plausible.

However, the differences between the Traders and Curry members may also reflect the differences in the composition and redox state of the oceans and atmosphere during their respective deposition times (Bekker et al., 2010, Canfield, 1998, Holland, 1984). Such differences may or may not be directly related to the changes in the depositional depth described in the previous paragraph. Since the Traders Member's magnetite appears to be created by the alteration of its clays and not reduction of hematite (as in the Curry Member), it could be hypothesized that the member's original depositional environment was different from that of the Curry Member. The oxygen, sulfate, and nitrate contents of the ocean's chemical state was in flux at this time. Perhaps the two members formed at different oceanic states wherein the amount of iron, manganese, and phosphorous rich soluble solution differed. This initial difference during the sedimentary phase of the Traders and Curry Members could be the reason for the difference in the magnetite to hematite ratio we see today.

These different depositional environments may also explain the Traders Member characteristic BIF appearance in contrast to the Curry Member more characteristically GIF appearance. The Traders Member exhibits more pronounced banding at all scales compared to the Curry Member. Furthermore, the Traders Member was uniformly oblate in its AMS shape, whereas the Curry Member had a mix of shapes, which is more likely in the less laminated GIFs. If the Traders Member is a BIF, and thus a deep water deposit that was then uplifted (perhaps by the South Range fault) to a shallow water (more oxidizing)

deposit forming the Curry Member GIF, that may explain the hematite to magnetite ratio difference between the members.

James (1955) suggested that both iron-bearing members underwent the same intermediate metamorphism based on their iron constituents. Examining the metamorphic facies of the members was not the goal of this study. However, our results could indicate the presence of different metamorphic facies. The iron oxides in BIF are generally considered postdepositional in origin (although this too is debated (Johnson et al., 2008) so since the Traders and Curry Members consist of different ratios of iron oxides they may have dissimilar metamorphic histories. Magnetite is thought to replace or overgrow hematite in BIFs (e.g. Ayers 1972; Ewers and Morris, 1981) during deep burial diagenesis. The domination of magnetite in the Traders Member could indicate different metamorphism. This theory is further supported by paleodirectional data. The Traders and Curry Members differ in both direction and inclination. This is usually indicative of different times of magnetic grain crystallization.

The obtained data on magnetic properties of the Traders and Curry Members will be useful for the interpretation of the anticipated aeromagnetic data to be obtained by the USGS in the future. The two most important parameters are the Koenigsberger ratio (the Q ratio) and the AMS characteristics. The low (≈1) Q-values observed for both members indicate that the magnetic anomalies over the rocks are a complex combination of induced and remanent magnetization. However, the observed anisotropy of magnetic susceptibility for both members indicates that the induced magnetization may deviate from the ambient magnetic field direction. Specifically, K1 and K3 are used to correct observed magnetization and inclination acquired by an aeromagnetic survey. Further analyses in this direction will require the actual aeromagnetic data.

6. Conclusion

The results of our magnetic petrophysical investigation of the Vulcan Iron Formation indicate that the iron-bearing Traders Member and Curry Member, are differentiable based on their magnetic characteristics and may in fact represent the two

different types of iron-formation – the banded iron formation (Traders) and granular iron formation (Curry). This contradicts the current view that the two members cannot be differentiated without outside geologic criteria. The members can be separated based on their relative ratios of magnetic minerals (hematite-to-magnetite). Magnetite dominate the Traders Member, whereas hematite dominates the Curry Member. The obtained data are important for interpretation of future aeromagnetic surveys over the Vulcan Formation and may be useful for understanding the depositional regimes and environmental conditions during the late Paleoproterozoic.

7. References

Abbott, D., and Isley, A. (2002). The intensity, occurrence, and duration of superplume events and eras over geological time, *Journal of Geodynamics*, v. 34, p. 265−307.

Ayres, D.E. (1972). Genesis of iron-bearing minerals in banded iron formation mesobands in the Dales Gorge Member, Hamersley Group, Western Australia. *Economic Geology*, v. 67, p. 1214−1233.

Barker, C. E., Pawlewicz, M., & Cobabe, E. A. (2001). Deposition of sedimentary organic matter in black shale facies indicated by the geochemistry and petrography of high-resolution samples, Blake Nose, western North Atlantic. *Geological Society, London, Special Publications*, 183(1), 49-72.

Bayley, R. W., Dutton, C. E., & Lamey, C. A. (1966). Geology of the Menominee iron-bearing district, Dickinson County, Michigan, and Florence and Marinette Counties, Wisconsin (No. 513). *US Govt. Print. Off.,.*

Bekker, A., Slack, J. F., Planavsky, N., Krapež, B., Hofmann, A., Konhauser, K. O., & Rouxel, O. J. (2010). Iron formation: the sedimentary product of a complex interplay among mantle, tectonic, oceanic, and biospheric processes. *Economic Geology*, 105(3), 467-508.

Butler, R. F. (1998). Paleomagnetism: Magnetic Domains to Geologic Terranes, *Electronic Edition*.

Canfield, D.E. (1998). A new model for Proterozoic ocean chemistry, *Nature*, v. 396, p. 450−453.

Cannon, W.F., Gair, J.E. (1970). A revision of stratigraphic nomenclature for middle Precambrian rocks in northern Michigan. *Geological Society of America Bulletin* 81, 2843–2846.

Chadima, M., and Hrouda, F. (2012). Thermomagnetic Curve Browser, Cureval 8.0.2 for Windows. Beta Version. AGICO, Inc., Brno, Czech Republic at www.agico.com.

Day, R., M. Fuller, and V. A. Schmidt (1977). Hysteresis properties of titanomagnetites: Grain-size and compositional dependence, *Phys. Earth Planet. Inter*., 13, 260–267.

Dunlop, D. J. (1974). Thermal enhancement of magnetic susceptibility. *J. Geophys*., 40, 439–451.

Ewers, W.E., and Morris, R.C. (1981). Studies of the Dales Gorge Member of the Brockman Iron Formation, Western Australia. *Economic Geology*, v. 76, p. 1929–1953.

Graham, C. D. (2000). High-Sensitivity Magnetization Measurements. J. Mater *Sci Technol* 16: 97-101.

Gross, G.A. (1980). A classification of iron-formation based on depositional environments. *Canadian Mineralogist*, v. 18, p. 215–222.

Guo, W. W., Li, Z. X., & Dentith, M. C. (2011). Magnetic petrophysical results from the Hamersley Basin and their implications for interpretation of magnetic surveys. *Australian Journal of Earth Sciences*, 58(4), 317-333.

Harrison,R. J., and J. M. Feinberg (2008). FORCinel: An improved algorithm for calculating first-order reversal curve distributions using locally weighted regression smoothing. *Geochem. Geophys. Geosyst*., 9, Q05016,doi:10.1029/2008GC001987.

Hoffman, P.F. (1987). Early Proterozoic foredeeps, foredeep magmatism, and Superior-type iron-formations of the Canadian Shield, in Kröner, A., ed., Proterozoic lithospheric evolution: Washington, D.C., American Geophysical Union, and Boulder, Colorado. *Geological Society of America*, p. 85−98.

Hoffman, P.F., Kaufman, A.J., Halverson, G.P., and Schrag, D.P. (1998). A Neoproterozoic snowball Earth. *Science*, v. 281, p. 1342−1346.

Holland, H.D. (1984). The chemical evolution of the atmosphere and oceans: New York, *Princeton University Press*, 582 p.

Holland, H.D. (2002). Volcanic gases, black smokers, and the Great Oxidation Event. *Geochim Cosmochim Acta,* 66(21):3811–3826.

Holland, H.D. (2005) Sedimentary mineral deposits and the evolution of Earth's near surface environments. *Economic Geology*, v. 100, p. 1489−1509.

Huston, D.L., and Logan, G.A. (2004). Barite, BIFs and bugs: Evidence for the evolution of the Earth's early hydrosphere. *Earth and Planetary Science Letters*, v. 220, p. 41−55.

James. H. L. (1955). Zones of regional metamorphism in the Precambrian of northern Michigan. *Geol. Soc. American Bull*., v. 66, no. 12, pt. 1, p. 1455-1488.

Jelinek, V. (1981). Characterization of the magnetic fabric of rocks. *Tectonophysics*, 79(3-4), T63-T67.

Klein, C. (2005) Some Precambrian Banded Iron-Formations (BIFs) From Around The World: Their Age, Geologic Setting, Mineralogy, Metamorphism, Geochemistry, And Origin. *Am. Min.* 90, 1473-1499.

Kosterov, A. A., and M. Prévot (1998). Possible mechanisms causing failure of Thellier palaeointensity experiments in some basalts. *Geophys. J. Int*., 134, 554–572.

Leith, C. K., Lund, R. J., and Leith, Andrew (1935). Precambrian rocks of the Lake Superior regions; a review of newly discovered geologic features with a revised geologic map. *U.S. Geol. Survey Prof. Paper* 184, 34 p.

Mayergoyz I D (1986). Mathematical models of hysteresis. *IEEE Trans. Magn*., vol. 22, pp. 603–608, doi: 10.1109/TMAG.1986.1064347.

Meurant, G. (2012). Handbook of Strata-Bound and Stratiform Ore Deposits, Volume 7, Au, U, Fe, Mn, Hg, Sb, W, and P Deposits. 143-152

Morey, G.B., & Southwick, D. L. (1995). Allostratigraphic relationships of Early Proterozoic Iron-formations in the Lake Superior region. *Economic Geology*, 90(7), 1983-1993.

Morin, F. J. (1950). Magnetic susceptibility of αFe2O3 and αFe2O with added titanium. *Physical Review*, 78(6), 819.

Mukherji, A., Chaudhuri, A. K., & Mamtani, M. A. (2004). Regional scale strain variations in Banded Iron Formations of eastern India: results from anisotropy of magnetic susceptibility studies. *Journal of Structural Geology*, 26(12), 2175-2189.

Özdemir, Ö., D. J. Dunlop, and B. M. Moskowitz (1993). The effect of oxidation on the Verwey transition in magnetite. *Geophys. Res. Lett*., 20, 1671–1674.

Pike, C. R., Roberts, A. P., & Verosub, K. L. (1999). Characterizing interactions in fine magnetic particle systems using first order reversal curves. *Journal of Applied Physics*, 85(9), 6660-6667.

Poulton, S.W., Fralick, P.W., and Canfield, D.E. (2004). The transition to a sulphidic ocean 1.84 billion years ago. *Nature*, v. 43, p. 173−177.

Roberts, A. C., Stirling, J. A., Grice, J. D., Frisch, T., Herd, R. K., & Jambor, J. L. (1993). Harrisonite, a new calcium iron silicate-phosphate from Arcedeckne Island, District of Franklin, Arctic Canada. *Canadian Mineralogist*, 31, 775-775.

Roberts, A. P., Pike, C. R., & Verosub, K. L. (2000). First-order reversal curve diagrams: A new tool for characterizing the magnetic properties of natural samples. *Journal of Geophysical Research: Solid Earth*, 105(B12), 28461-28475.

Schulz, K.J., and Cannon, W.F. (2007). The Penokean orogeny in the Lake Superior region. *Precambrian Research*, v. 157, p. 4–25.

Simonson, B.M., and Goode, A.D.T. (1989). First discovery of ferruginous chert arenites in the early Precambrian Hamersley Group of Western Australia. *Geology*, v. 17, p. 269−272.

Simonson, B.M., and Hassler, S.W. (1996). Was the deposition of large Precambrian iron formations linked to major marine transgressions? *Journal of Geology*, v. 104, p. 665−676.

Sims, P.K. and Schulz, K.J. (1993). Geologic map of Precambrian rocks of parts of Iron Mountain and Escanaba 30’ x 60’ quadrangles, Northern Wisconsin and adjacent Michigan [map]. (ca. 1:100,000.) U.S. Department of the Interior

Tarling, D., & Hrouda, F. (Eds.). (1993). Magnetic anisotropy of rocks. *Springer Science & Business Media*.

Verwey, E. J. W., 1939. Electron Conduction of Magnetite (Fe3O4) and its Transition Point at Low Temperatures. Nature, 144, 327-328.